The Astrophysical Journal, 784:9 (22pp), 2014 March 20 doi:10.1088/0004-637X/784/1/9

IS THERE A MAXIMUM STAR FORMATION RATE IN HIGH-REDSHIFT GALAXIES?*,†,‡,§

A. J. Barger[1,2,3], L. L. Cowie[3], C.-C. Chen[3,4], F. N. Owen[5], W.-H. Wang[6], C. M. Casey[3,7], N. Lee[3], D. B. Sanders[3], and J. P. Williams[3]
[1] Department of Astronomy, University of Wisconsin-Madison, 475 N. Charter Street, Madison, WI 53706, USA
[2] Department of Physics and Astronomy, University of Hawaii, 2505 Correa Road, Honolulu, HI 96822, USA
[3] Institute for Astronomy, University of Hawaii, 2680 Woodlawn Drive, Honolulu, HI 96822, USA
[4] Institute for Computational Cosmology, Durham University, South Road, Durham DH1 3LE, UK
[5] National Radio Astronomy Observatory, P.O. Box O, Socorro, NM 87801, USA
[6] Academia Sinica Institute of Astronomy and Astrophysics, P.O. Box 23-141, Taipei 10617, Taiwan
[7] Department of Physics and Astronomy, University of California at Irvine, 2162 Frederick Reines Hall, Irvine, CA 92697, USA
Received 2013 November 11; accepted 2013 December 24; published 2014 February 26

ABSTRACT

We use the James Clerk Maxwell Telescope's SCUBA-2 camera to image a 400 arcmin^2 area surrounding the GOODS-N field. The 850 μm rms noise ranges from a value of 0.49 mJy in the central region to 3.5 mJy at the outside edge. From these data, we construct an 850 μm source catalog to 2 mJy containing 49 sources detected above the 4σ level. We use an ultradeep (11.5 μJy at 5σ) 1.4 GHz image obtained with the Karl G. Jansky Very Large Array together with observations made with the Submillimeter Array to identify counterparts to the submillimeter galaxies. For most cases of multiple radio counterparts, we can identify the correct counterpart from new and existing Submillimeter Array data. We have spectroscopic redshifts for 62% of the radio sources in the 9′ radius highest sensitivity region (556/894) and 67% of the radio sources in the GOODS-N region (367/543). We supplement these with a modest number of additional photometric redshifts in the GOODS-N region (30). We measure millimetric redshifts from the radio to submillimeter flux ratios for the unidentified submillimeter sample, assuming an Arp 220 spectral energy distribution. We find a radio-flux-dependent $K - z$ relation for the radio sources, which we use to estimate redshifts for the remaining radio sources. We determine the star formation rates (SFRs) of the submillimeter sources based on their radio powers and their submillimeter fluxes and find that they agree well. The radio data are deep enough to detect star-forming galaxies with SFRs >2000 $M_\odot$ yr^{-1} to $z \sim 6$. We find galaxies with SFRs up to ∼6000 $M_\odot$ yr^{-1} over the redshift range $z = 1.5$–6, but we see evidence for a turn-down in the SFR distribution function above 2000 $M_\odot$ yr^{-1}.

Key words: cosmology: observations – galaxies: active – galaxies: distances and redshifts – galaxies: evolution – galaxies: high-redshift – galaxies: starburst

Online-only material: color figures, machine-readable table

1. INTRODUCTION

Finding the galaxies that have the highest star formation rates (SFRs) at high redshifts has been a difficult problem. Such galaxies cannot be easily picked out in rest-frame ultraviolet (UV) or optical samples due to their very large and highly variable extinctions (e.g., Bouwens et al. 2009; Reddy et al. 2012), and though they can be found in far-infrared (FIR) or submillimeter selected galaxy samples, the poor resolution of single-dish submillimeter telescopes makes their interpretation complex. In particular, recent follow-up surveys with submillimeter interferometers have shown that at least some of the brightest submillimeter galaxies (SMGs) are blends of fainter sources with lower SFRs (e.g., Wang et al. 2011; Smolčić et al. 2012; Barger et al. 2012; Hodge et al. 2013b). In fact, Karim et al. (2013) suggested that almost all bright (>9 mJy) SMGs are blends and that there is a natural upper limit of ∼1000 $M_\odot$ yr^{-1} on the SFRs of galaxies.

One thing all SMG studies agree on is that there is a large fraction of cosmic star formation hidden by dust (e.g., Barger et al. 2000, 2012; Lagache et al. 2005; Chapman et al. 2005; Wang et al. 2006; Serjeant et al. 2008; Wardlow et al. 2011; Casey et al. 2013), most of which is occurring in the most massively star-forming galaxies in the universe. Thus, the construction of a complete picture of galaxy evolution requires a full understanding of galaxies at both optical and FIR/submillimeter wavelengths. However, in order to develop this understanding of the dusty universe, we need large, uniformly selected samples with well determined star-forming properties.

In this paper, we work toward this goal using a combination of powerful new data on the heavily studied Great Observatories Origins Deep Survey-North (GOODS-N; Giavalisco et al. 2004)/Chandra Deep Field-North (CDF-N; Alexander et al. 2003) field. We begin with a new, uniformly selected sample of 850 μm galaxies observed with the SCUBA-2 camera (Holland et al. 2013) on the 15 m James Clerk Maxwell Telescope (JCMT). Then, using a combination of extremely deep Karl G. Jansky Very Large Array (VLA) 1.4 GHz observations

* The James Clerk Maxwell Telescope is operated by the Joint Astronomy Centre on behalf of the Science and Technology Facilities Council of the United Kingdom, the National Research Council of Canada, and (until 2013 March 31) the Netherlands Organisation for Scientific Research.
† The National Radio Astronomy Observatory is a facility of the National Science Foundation operated under cooperative agreement by Associated Universities, Inc.
‡ The Submillimeter Array is a joint project between the Smithsonian Astrophysical Observatory and the Academia Sinica Institute of Astronomy and Astrophysics and is funded by the Smithsonian Institution and the Academia Sinica.
§ The W. M. Keck Observatory is operated as a scientific partnership among the California Institute of Technology, the University of California, and NASA, and was made possible by the generous financial support of the W. M. Keck Foundation.

(F. N. Owen, 2014, in preparation; hereafter, Owen14) and high-resolution Submillimeter Array (SMA; Ho et al. 2004) 860 μm observations, we analyze the fraction of SMGs that are single sources and estimate the SFR distribution function for the most massively star-forming galaxies in the universe.

The principal underpinning of this work is the new submillimeter imaging capability provided by SCUBA-2. SCUBA-2 covers 16 times the area of SCUBA (Holland et al. 1999) and has a mapping speed that is considerably faster than SCUBA, which means that large samples of SMGs can be obtained in only a few nights of observations. Previous samples of SMGs in the GOODS-N/CDF-N field were based on mosaics of SCUBA fields that only partially covered the area and that had widely varying sensitivities. SCUBA-2 enables the development of uniform, deep SMG samples over the entire field.

In order to construct the SFR distribution function, we need to determine how many of the SCUBA-2-selected sources are multiples, where the observed flux is a blend of two or more individual galaxies. High spatial resolution follow-up of bright SMGs at the same wavelength is now possible with the SMA or the Atacama Large Millimeter/submillimeter Array (ALMA), but the level of multiplicity is still somewhat controversial, particularly for the brightest SMGs (see Chen et al. 2013 for a full discussion).

As an illustration of the different results that have been obtained, Karim et al. (2013) found that all of the brightest (>12 mJy) sources in their LABOCA Extended Chandra Deep Field-South Submillimeter Survey that they successfully detected with their targeted ALMA observations were composed of emission from multiple fainter SMGs, each with 870 μm fluxes of $\lesssim$9 mJy. (Note that of the 88 "best" ALMA maps used in their analysis, 19 contained no >3.5σ detections.) They also did not find any ALMA sources with fluxes >9 mJy. In contrast, Barger et al. (2012) confirmed with the SMA three single sources in the GOODS-N field with fluxes >9 mJy, two of which had fluxes $\gtrsim$12 mJy. The differences may be partly explainable as a purely observational blending effect due to the different beam sizes of the single-dish submillimeter telescopes used to construct the SMG samples (14″ for SCUBA versus 19.″2 for LABOCA). However, this emphasizes the importance of determining the multiplicity level for the specific sample that is being used.

In this paper, we approach the multiplicity issue in two ways. Our first approach is the most direct: submillimeter interferometric imaging of the SCUBA-2 selected SMGs. Such follow-up observations can localize the submillimeter emission extremely accurately and allow the determination of whether the SMG is a single source or a blend (e.g., Iono et al. 2006; Wang et al. 2007, 2011; Younger et al. 2008a, 2008b; Cowie et al. 2009; Hatsukade et al. 2010; Knudsen et al. 2010; Chen et al. 2011; Barger et al. 2012; Karim et al. 2013; Hodge et al. 2013b). We have used the SMA to measure the properties of a very large fraction of the SMGs in the SCUBA-2 sample, including many of the brightest ones.

Our second approach is to use 1.4 GHz observations to identify the counterparts to the SMGs. Historically, this approach has been less than ideal, because it introduced a strong bias against high-redshift SMGs due to the positive K-correction of the radio synchrotron emission and the negative K-correction of the submillimeter thermal dust emission. However, with the upgraded VLA, 1.4 GHz images (Owen14) are now deep enough to find counterparts to nearly all of the SCUBA (Barger et al. 2012) or SCUBA-2 (this paper) sources, removing the radio bias. Thus, for most of the SCUBA-2 galaxies without SMA data, we can identify single radio sources as their counterparts.

It is also possible to identify high SFR galaxies directly in the radio, though this is complicated by the fact that many high radio power sources are active galactic nuclei (AGNs) rather than star formers. Radio galaxies pick out high-mass galaxies, as can be seen from the "$K-z$ relation," a well-known tight correlation between the K-band magnitudes of radio host galaxies and their redshifts that was discovered by Lilly & Longair (1984) using the bright 3CRR survey (Laing et al. 1983) and confirmed with lower power radio surveys (e.g., Eales et al. 1997 using the 6CE; Jarvis et al. 2001 using the 6C*; Lacy et al. 2000 using the 7C-III). At an order of magnitude even fainter than the above surveys, De Breuck et al. (2002) found that their $S_{1.4\,\mathrm{GHz}} > 10$ mJy sample of ultra-steep-spectrum radio sources also followed the $K-z$ relation and traced the bright K-band envelope of field galaxies out to $z \lesssim 1$ before becoming $\gtrsim$2 mag brighter at higher redshifts. This led them to conclude that the radio galaxies were pinpointing the most massive systems at all redshifts.

Clearly, the $K-z$ relation has important implications for the formation of massive galaxies. Willott et al. (2003; hereafter, Willott03) combined the 7C Redshift Survey (7CRS) with the 3CRR, 6CE, and 6C* samples and found that the shape of the $K-z$ relation is closely approximated by the magnitude–redshift relation for an elliptical galaxy that formed at $z = 10$. Rocca-Volmerange et al. (2004) modeled the $K-z$ relation using magnitudes computed for a fixed baryonic mass galaxy with an elliptical (fast conversion of gas to stars) star formation history starting at high redshift ($z = 10$). In their interpretation, the most powerful radio sources are in galaxies with baryonic masses of $\sim 10^{12}\ M_\odot$, while lower radio power sources are in galaxies with slightly smaller baryonic masses. Rocca-Volmerange et al.'s adopted elliptical star formation timescale for this model (1 Gyr) would imply SFRs $\sim$1000 $M_\odot$ yr^{-1} in all luminous radio galaxies at $z \gtrsim 4$.

The primary science goals of the present paper are to estimate for the most massively star-forming galaxies in the universe (1) the highest SFRs, (2) the distribution of SFRs, and (3) the contribution to the universal star formation history and how that contribution compares to the contribution from extinction-corrected UV-selected samples. The structure of the paper is as follows. In Section 2, we discuss the GOODS-N/CDF-N imaging data sets that we use, including SCUBA-2, radio, SMA, K_s, and X-ray. We construct both a >4σ SCUBA-2 850 μm catalog and an SMA 860 μm catalog using all available data. We identify radio counterparts to the SMGs and give their K_s magnitudes, as well as their spectroscopic and photometric redshifts, where available. We measure millimetric redshifts from the radio to submillimeter flux ratios assuming an Arp 220 spectral energy distribution (SED). In Section 3, we show the redshift distribution of the radio sample. In Section 4, we present the $K-z$ relation for our sample and use it to estimate additional redshifts. In Section 5, we focus on the high radio power sources in the sample and how the SMGs are drawn from this population. We also describe our conversions of the 1.4 GHz powers and submillimeter fluxes into SFRs. In Section 6, we use our SCUBA-2 sample to determine the SFR distribution function at $z = 1.5$–6 and to construct the star formation history, which we compare with the history determined from extinction-corrected UV samples. In Section 7, we discuss the implications of our results, and in Section 8, we summarize the paper.

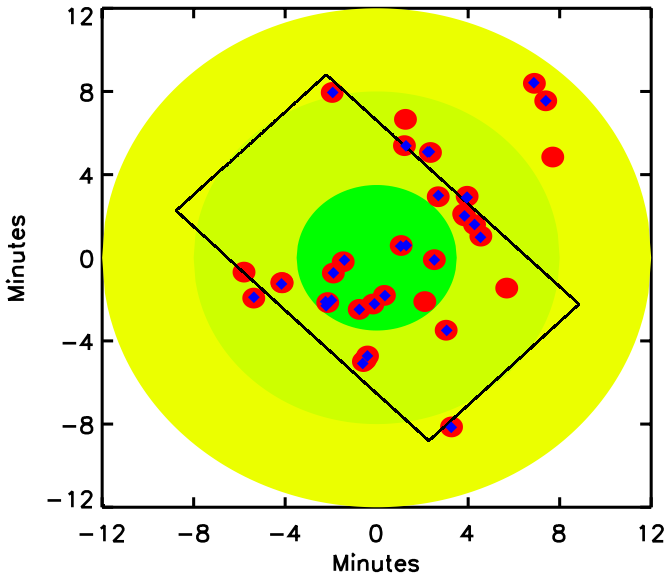

Figure 1. GOODS-N/CDF-N SCUBA-2 field obtained with the CV Daisy scanning mode (dark green—area with the highest sensitivity, light green—area where the rms noise is <4 times the central sensitivity) and the pong-900 scanning mode (yellow shading). The black rectangle shows the GOODS-N *HST* ACS field. The red circles (24″ radius to show the area where the rms noise is <3 times the central sensitivity) denote the 28 SMA fields in the region (see Section 2.3); note that some of the SMA fields overlap. The blue diamonds mark the >4σ SMA detections in the SMA fields.

(A color version of this figure is available in the online journal.)

We adopt the AB magnitude system for the optical and NIR photometry, and we assume the Wilkinson Microwave Anisotropy Probe cosmology of $H_0 = 70.5$ km s^{-1} Mpc^{-1}, $\Omega_M = 0.27$, and $\Omega_\Lambda = 0.73$ (Larson et al. 2011) throughout.

2. DATA

2.1. SCUBA-2 Imaging

We obtained 25.4 hr of observations on the CDF-N with SCUBA-2 on the JCMT during observing runs in 2012 and 2013. The data were obtained using a mixture of scanning modes and under a variety of weather conditions. Using the CV Daisy scanning mode (detailed information about the SCUBA-2 scan patterns can be found in Holland et al. 2013), we obtained a 2.2 hr observation in band 1 weather (225 GHz opacity < 0.05) and a 16.5 hr observation in band 2 weather (225 GHz opacity ~0.05–0.08). We also obtained a 6.7 hr observation in band 2 weather using the pong-900 scanning mode. While SCUBA-2 observes at both 450 μm and 850 μm simultaneously, there are too few sources directly detected at 450 μm in our data to be interesting. Thus, we only use the 850 μm data in our subsequent analysis.

In terms of the two scanning modes, CV Daisy is optimal for going deep on small areas (<4′ radius), while pong-900 provides a uniform rms over a large area (<12′ radius). In Figure 1, we compare the CV Daisy field (dark green shading indicates the area with the highest sensitivity, and light green shading indicates the area where the rms noise is less than four times the central sensitivity) with the pong-900 field (yellow shading). To illustrate the size of the SCUBA-2 images, the black rectangle shows the GOODS-N *Hubble Space Telescope* (*HST*) Advanced Camera for Surveys (ACS) coverage.

We took darks and flat fields at the beginning and end of each scan. We did Skydips at least twice per night in order to calculate the opacity factors. We reduced the data using the Dynamic Iterative Map-Maker (DIMM) in the SMURF package from the STARLINK software developed by the Joint Astronomy Centre. We calibrated the fluxes using the standard flux conversion factor for 850 μm of 537 Jy pW^{-1}. The relative calibration accuracy is expected to be stable and good to 5% at 850 μm (Dempsey et al. 2013). For more details on the GOODS-N/CDF-N SCUBA-2 data reduction and flux calibration, we refer the reader to Chen et al. (2013).

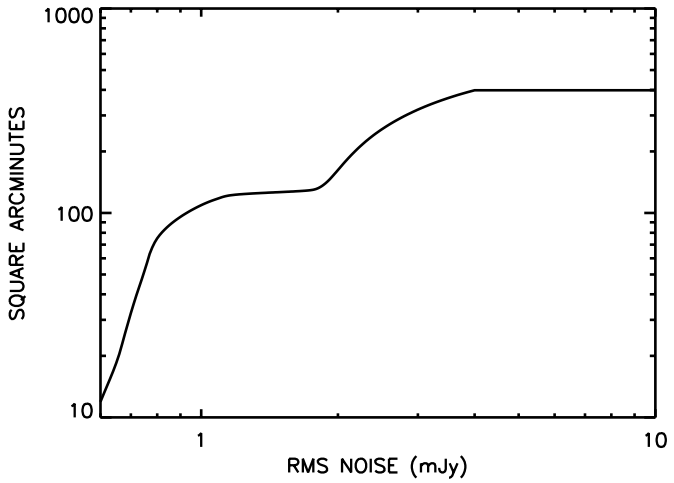

Figure 2. Area vs. rms noise of the combined GOODS-N/CDF-N SCUBA-2 pong-900 and CV Daisy 850 μm maps.

We combined the pong-900 map with only the portion of the CV Daisy map contained within the dark and light green shaded regions of Figure 1 to avoid damaging the sensitivity of the pong-900 map further out where the Daisy coverage is sparse. Nearly all of the SMGs are expected to be compact relative to the beam size of the JCMT at 850 μm. In order to increase the detectability of these point sources, we applied a matched-filter to our maps, which is a maximum likelihood estimator of the source strength (e.g., Serjeant et al. 2003a). The point-spread function (PSF) for the matched-filter algorithm should ideally be a Gaussian normalized to a peak of unity with FWHM equal to the JCMT beam size (14″ at 850 μm). However, the map produced from DIMM typically has low spatial frequency structures that need to be subtracted off before source extraction can be done. Thus, before running the matched-filter, we convolved the map with a broad Gaussian (30″ FWHM) normalized to a sum of unity, and we subtracted this convolved map from the original map. The resulting PSF is a Gaussian with a broader Gaussian subtracted off, giving a Mexican hat-like wavelet. We show the area versus rms noise in the matched-filter 850 μm image in Figure 2.

We first extracted sources having a peak signal-to-noise ratio (S/N) greater than 3.0. We did this by finding the maximum pixel in the matched-filter image. We then used the position and flux of the source at that peak to subtract a PSF that we centered at that position and scaled to match the flux. We iterated this process of identifying and removing sources until there were no remaining peak S/N values greater than 3.0. We treated the >3σ peaks as the preliminary catalog. In forming the final catalog, we kept every >4σ source in the preliminary catalog.

In Figure 3, we mark on the SCUBA-2 map the 850 μm > 4σ catalog sources (large circles). Hereafter, we refer to this as our SCUBA-2 sample. In Table 1, we present the sample in tabular form. In Column 1, we give our CDF-N name for the source. Where a GOODS 850 number from Wang et al. (2004) or a GN number from Pope et al. (2005) exists, we give that name in parentheses. In Columns 2 and 3, we give

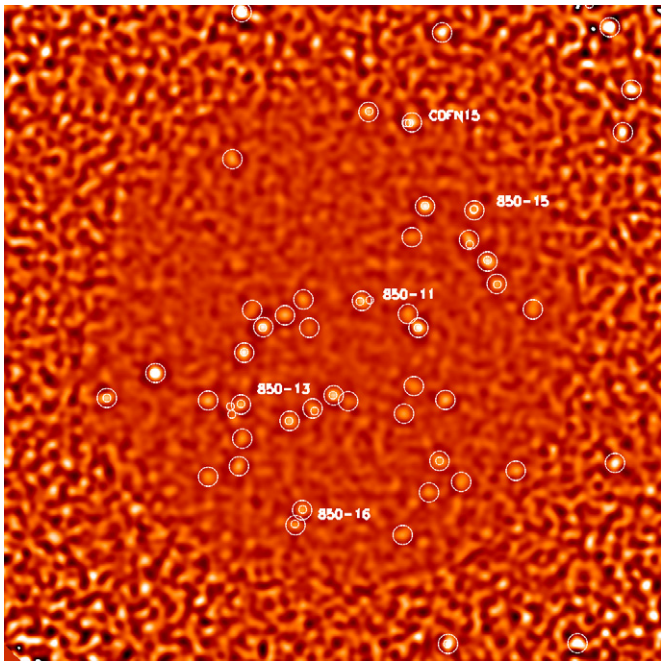

Figure 3. 850 μm $> 4\sigma$ catalog sources marked on the SCUBA-2 map (large circles). The portion of the map shown is 16.′7 on a side. The SMA detections (see Section 2.3) are shown with smaller circles. Sources that were single detections in the SCUBA survey of Wang et al. (2004) but then were observed to split into multiples in the SMA data are labeled with the Wang et al. name. (Note that the GOODS 850-15 multiple is very close; see Figure 14 in Barger et al. 2012.) In some cases (GOODS 850-13 and GOODS 850-16), the new SCUBA-2 data also separate the sources. (Note, however, that two of the three SMA sources making up GOODS 850-13 lie below the SCUBA-2 detection threshold.)

(A color version of this figure is available in the online journal.)

the J2000 right ascensions and declinations from the SCUBA-2 data. We have ordered the catalog by decreasing 850 μm flux, which we give in Column 4. In Columns 5 and 6, we list the 850 μm 1σ errors and S/N ratios, respectively. For the sources detected at 860 μm with the SMA, in Column 7, we give the SMA fluxes with the 1σ errors in parentheses. In Column 8, we give the 1.4 GHz fluxes with the 1σ errors in parentheses, and in Columns 9 and 10, we give the J2000 right ascensions and declinations from the radio data. Where more than one radio source lies within the SCUBA-2 beam, and where there are no SMA observations to determine the true radio counterpart, we list both radio sources. We list the K_s magnitudes in Column 11, and we give the spectroscopic (including CO), photometric, and millimetric redshifts in Columns 12–14.

2.2. Radio Imaging

Owen14 constructed a catalog of 1.4 GHz sources detected in the VLA image of the GOODS-N/CDF-N field. The image covers a 40′ diameter region with an effective resolution of 1.″8. The absolute radio positions are known to 0.″1–0.″2 rms. The highest sensitivity region is about 9′ in radius, producing a relatively uniform radio map with an rms of 2.3 μJy. We refer to this region as the full field in the rest of the paper. There are 894 distinct radio sources in this region, excluding sources that appear to be parts of other sources.

2.3. SMA Imaging

There are 28 fields within ±9.′5 of the GOODS-N center that have been observed with the SMA. Most of these observations were targeted on SCUBA 850 μm sources or, more recently, SCUBA-2 850 μm sources, primarily by our own group (24 of the 28 fields). Of these, 12 were presented in Wang et al. (2011) and Barger et al. (2012), while Chen et al. (2013) used our full sample to analyze the effects of multiplicity on the number counts. We show all 28 SMA fields (some of which are overlapped) in Figure 1 as the red circles. Taken together, they cover ∼14 arcmin^2.

There are 16 images not already analyzed in Wang et al. (2011) and Barger et al. (2012). For one of these images (GN20), we simply adopted the SMA 890 μm flux and error presented in Iono et al. (2006). For the others, we calibrated and inspected the SMA 860 μm data using the IDL-based Caltech package MIR modified for the SMA, as in our previous work.

Considering only the regions in each image where the noise was less than four times the minimum noise, we searched all of the SMA images (except for the one containing GN20) for sources detected above the 4σ threshold. Including GN20, there are 29 such sources, which we mark in Figure 1 with blue diamonds. These sources were all the intended targets of the SMA observations. Apart from the multiples, we found no serendipitous sources in the fields. Chen et al. (2013) compared the SMA and SCUBA-2 fluxes for the sources and found that most agree statistically (see their Figure 10).

We compare the SMA (small circles) and SCUBA-2 (large circles) detections in Figure 3. All of the SCUBA-2 sources observed with the SMA were detected. We find that only three of the SCUBA-2 sources, CDFN16 (GOODS 850-11), CDFN37 (GOODS 850-15), and CDFN15, have multiple counterparts in the SMA images. Two previous SCUBA sources (GOODS 850-13 and GOODS 850-16) that were blends of SMA sources are separated in the SCUBA-2 data into individual sources. (Note, however, that two of the three SMA sources making up GOODS 850-13 lie below the SCUBA-2 detection threshold.)

With our accurate SMA positions, we can unambiguously determine the radio counterparts to the SMGs. Indeed, we find radio counterparts above the 1.4 GHz threshold of ∼11.5 μJy (5σ) for all of the SMA sources, except CDFN15a and CDFN15b. We show one example in Figure 4. There are four radio sources in the SMA field (small circles), but only one of them is the clear counterpart to the SMA source. The other three have no significant submillimeter flux.

We tested the astrometric accuracy of the SMA observations relative to the Owen14 1.4 GHz sample and found that they are in perfect astrometric agreement. The dispersion in the positional offsets is 0.″5.

In Table 2, we summarize the properties of the 29 SMA sources. In Column 1, we give the name from the literature or, for new sources, the name from our SCUBA-2 catalog (Table 1). In Columns 2 and 3, we give the J2000 right ascensions and declinations for each source as measured from the SMA data. In Column 4, we list the SMA 860 μm fluxes and 1σ errors. In Column 5, we give the references for the SMA data. In Column 6, we list the 1.4 GHz fluxes and 1σ errors from Owen14. These are peak fluxes when the peak flux equals the extended flux and extended fluxes otherwise. In Column 7, we give the spectroscopic redshifts as found in the literature. In Column 8, we give the references for those spectroscopic measurements.

2.4. Near-infrared Imaging

Wang et al. (2010) constructed a K_s catalog of the GOODS-N/CDF-N field, which they publicly released along with the extremely deep Canada–France–Hawaii Telescope K_s image from which the catalog was extracted. In the GOODS-N region,

Table 1
SCUBA-2 Sample

Name	R.A. (850 μm) J2000.0 (^{h} ^{m} ^{s})	Decl. (850 μm) J2000.0 ($^\circ$ $'$ $''$)	Flux 850 μm (mJy)	Error 850 μm (mJy)	S/N	SMA 860 μm (mJy)	Flux 1.4 GHz (μJy)	R.A. (1.4 GHz) J2000.0 (^{h} ^{m} ^{s})	Decl. (1.4 GHz) J2000.0 ($^\circ$ $'$ $''$)	K_s (AB)	$z_{\rm spec}$	$z_{\rm phot}$	$z_{\rm milli}$
(1)	(2)	(3)	(4)	(5)	(6)	(7)	(8)	(9)	(10)	(11)	(12)	(13)	(14)
CDFN1	12 35 55.53	62 22 36.56	16.95	3.45	4.92	17.0(1.9)	58.5(7.6)	12 35 55.88	62 22 39.0	22.12	...		3.624
CDFN2	12 35 51.51	62 21 46.07	16.90	3.16	5.35	13.7(2.8)	51.9(7.3)	12 35 51.37	62 21 47.2	22.11	...		3.447
CDFN3 (GN20)	12 37 11.92	62 22 09.31	16.41	2.26	7.27	23.9(2.5)	87.50(15.)	12 37 11.89	62 22 12.7	22.69	4.055	4.125	3.487
CDFN4 (850-6)	12 37 30.53	62 12 59.30	12.21	0.77	15.81	14.9(0.9)	126.0(4.9)	12 37 30.80	62 12 58.7	22.92	...	2.627	2.504
CDFN5	12 35 58.96	62 06 07.16	11.90	2.83	4.21		<7.5						
CDFN6	12 35 46.74	62 20 10.76	11.13	2.74	4.06		53.40(12.)	12 35 47.06	62 20 9.70	18.97	0.543	0.568(R)	
							85.7(6.7)	12 35 46.64	62 20 13.3	22.75	...		
CDFN7	12 35 48.70	62 19 05.41	10.27	2.43	4.23		71.3(6.4)	12 35 48.84	62 19 4.91	22.85			2.792
CDFN8	12 36 26.98	62 06 06.27	9.46	2.29	4.13	11.5(0.7)	34.20(2.9)	12 36 27.21	62 06 5.59	24.84	...		3.697
CDFN9	12 36 28.16	62 21 38.46	9.09	2.20	4.13		35.60(3.2)	12 36 28.67	62 21 39.7	20.39	1.194	1.191(R)	3.160
CDFN10	12 35 50.72	62 10 41.78	8.69	2.09	4.16		25.00(3.0)	12 35 50.35	62 10 41.9	23.60			3.638
CDFN11 (850-5/GN10)	12 36 33.41	62 14 08.10	8.24	0.63	13.06	12.0(1.4)	33.20(5.6)	12 36 33.38	62 14 8.40	26.59	4.042	...	3.373
CDFN12	12 36 31.86	62 17 12.97	7.84	0.71	10.99	7.1(0.5)	21.60(2.5)	12 36 31.94	62 17 14.5	23.04	...	3.757	3.620
CDFN13 (850-36)	12 37 11.29	62 13 29.89	7.74	0.65	11.89	6.7(0.6)	123.8(5.4)	12 37 11.34	62 13 30.9	20.45	1.995	1.801	1.893
CDFN14 (850-9/GN19)	12 37 07.11	62 14 09.08	7.62	0.57	13.27	7.1(1.4)	58.40(11.)	12 37 7.210	62 14 7.91	21.44	2.490	2.451(R)	2.488
CDFN15	12 36 34.70	62 19 21.37	7.13	0.98	7.29	(a) 7.2(1.7)	<7.2						
						(b) 6.8(1.7)	<7.2						
CDFN16 (850-3/GN6)	12 36 18.24	62 15 48.98	7.12	0.77	9.25	7.2(0.7)	163.6(4.9)	12 36 18.35	62 15 50.4	22.02	2.000	2.508	1.333
CDFN17 (850-1/GN14)	12 36 51.83	62 12 25.79	6.04	0.55	11.01	7.8(1.0)	12.50(2.4)	12 36 52.03	62 12 25.9	99.00	5.183	...	4.277
CDFN18	12 37 41.20	62 12 21.21	5.74	0.99	5.77	7.1(1.8)	27.40(3.1)	12 37 41.18	62 12 21.0	23.36	...	3.029(R)	3.396
CDFN19	12 36 44.15	62 19 37.19	5.66	0.97	5.82	6.4(1.1)	25.40(2.9)	12 36 44.08	62 19 38.7	23.88	...		3.059
CDFN20 (850-11/GN12)	12 36 45.68	62 14 49.61	5.44	0.53	10.22	(a) 4.2(0.8)	101.0(2.5)	12 36 46.08	62 14 48.5	22.43	...	3.167	1.517
						(b) 5.3(1.1)	30.80(2.3)	12 36 44.03	62 14 50.5	21.52	2.095	1.754	2.819
CDFN21 (850-2/GN9)	12 36 22.26	62 16 22.37	5.16	0.76	6.75	9.3(1.4)	26.10(6.1)	12 36 22.10	62 16 15.9	23.92	...	...	3.600
CDFN22 (GN17)	12 37 01.35	62 11 46.10	5.04	0.65	7.79	4.8(0.6)	95.20(5.6)	12 37 1.593	62 11 46.4	20.57	1.73	1.868	1.791
CDFN23	12 36 27.57	62 12 18.03	4.89	0.70	6.98		17.50(2.5)	12 36 27.55	62 12 17.9	24.74	...	...	3.536
CDFN24	12 37 19.11	62 12 17.80	4.87	0.78	6.25		16.00(2.7)	12 37 18.96	62 12 17.5	23.13	...	...	
							12.60(2.5)	12 37 19.59	62 12 20.7	21.89	...		
CDFN25	12 37 12.41	62 10 37.76	4.66	0.74	6.32		23.00(2.4)	12 37 12.48	62 10 35.6	23.51	...	...	3.029
CDFN26	12 37 02.38	62 14 27.82	4.62	0.53	8.69		18.20(2.5)	12 37 2.600	62 14 26.9	22.25	3.214	2.949(R)	3.340
CDFN27	12 37 11.95	62 12 11.66	4.62	0.74	6.25	5.3(0.9)	33.00(2.4)	12 37 12.07	62 12 11.9	22.07	2.914	2.738	2.633
CDFN28 (GN4)	12 37 13.92	62 18 25.38	4.49	0.82	5.45		625.8(4.8)	12 37 13.89	62 18 26.2	24.41	...	...	0.745
CDFN29 (850-7)	12 36 16.30	62 15 15.32	4.38	0.77	5.72	3.4(0.6)	36.90(2.6)	12 36 16.10	62 15 13.8	22.24	2.578	2.940	2.344
CDFN30	12 36 12.18	62 10 30.18	4.34	0.97	4.46		26.50(5.3)	12 36 11.51	62 10 33.8	21.49	...	2.461	2.531
CDFN31 (GN11)	12 36 36.50	62 11 57.93	4.04	0.70	5.74		24.30(6.2)	12 36 36.14	62 11 54.3	22.87	...	0.628	2.712
CDFN32 (850-17)	12 36 28.85	62 10 45.69	4.04	0.78	5.15	7.7(0.9)	48.10(8.2)	12 36 28.90	62 10 45.2	22.96	...		2.766
CDFN33 (850-16a)	12 36 58.67	62 09 30.47	4.00	0.76	5.28	4.6(0.6)	27.50(2.6)	12 36 58.55	62 09 31.4	24.13	...	...	2.915
CDFN34 (850-15/GN7)	12 36 21.20	62 17 07.02	4.00	0.79	5.05	(a) 3.4(0.6)	164.6(5.0)	12 36 21.28	62 17 8.49	21.99	...		1.402
						(b) 3.5(0.7)	44.90(2.7)	12 36 20.98	62 17 9.80	21.64	1.988	2.016(R)	2.086

Table 1
(Continued)

Name	R.A. (850 μm) J2000.0 (^{h} ^{m} ^{s})	Decl. (850 μm) J2000.0 ($^{\circ}$ $'$ $''$)	Flux 850 μm (mJy)	Error 850 μm (mJy)	S/N	SMA 860 μm (mJy)	Flux 1.4 GHz (μJy)	R.A. (1.4 GHz) J2000.0 (^{h} ^{m} ^{s})	Decl. (1.4 GHz) J2000.0 ($^{\circ}$ $'$ $''$)	K_s (AB)	$z_{\rm spec}$	$z_{\rm phot}$	$z_{\rm milli}$
(1)	(2)	(3)	(4)	(5)	(6)	(7)	(8)	(9)	(10)	(11)	(12)	(13)	(14)
CDFN35	12 36 36.77	62 08 52.67	3.89	0.86	4.54		79.70(5.1)	12 36 37.03	62 08 52.4	22.01	...	2.139(R)	1.868
CDFN36	12 36 58.36	62 14 51.60	3.83	0.53	7.28		30.40(2.6)	12 36 57.82	62 14 55.0	19.78	0.849	0.822	2.137
CDFN37 (850-12/GN15)	12 36 56.35	62 12 05.29	3.82	0.59	6.51	4.5(0.8)	25.60(6.4)	12 36 55.85	62 12 1.29	21.52	2.737	1.904	2.583
CDFN38	12 37 11.71	62 11 19.34	3.75	0.75	5.03		<6.8						
CDFN39	12 36 31.07	62 09 57.24	3.68	0.80	4.58		148.8(4.8)	12 36 31.27	62 09 57.6	21.74	...	...	1.445
CDFN40	12 37 19.08	62 10 21.32	3.62	0.78	4.61		23.80(2.5)	12 37 19.55	62 10 21.2	24.10	...		2.743
CDFN41	12 36 24.05	62 10 13.63	3.56	0.82	4.36		38.50(2.6)	12 36 24.32	62 10 17.1	24.31	...	...	2.154
CDFN42	12 36 35.69	62 14 29.29	3.49	0.61	5.68		82.40(4.8)	12 36 35.59	62 14 24.0	20.16	2.005	2.046(R)	
							37.70(4.8)	12 36 35.87	62 14 36.0	21.11	1.018	1.151	
CDFN43	12 36 08.51	62 14 36.20	3.48	0.84	4.14		41.20(2.5)	12 36 8.598	62 14 35.4	22.66	...	...	
							22.00(2.7)	12 36 8.920	62 14 30.7	21.68	0.849	0.822	
CDFN44 (850-16b/GN16)	12 37 00.09	62 09 06.98	3.45	0.80	4.29	3.1(0.6)	297.2(5.0)	12 37 0.270	62 09 9.70	21.85	...	...	0.892
CDFN45	12 36 34.42	62 12 39.14	3.04	0.66	4.65		185.8(5.0)	12 36 34.51	62 12 40.9	19.98	1.224	1.247	1.097
CDFN46	12 36 34.81	62 16 26.06	2.82	0.69	4.07		52.70(6.2)	12 36 34.87	62 16 28.4	19.80	0.847	0.893	1.911
CDFN47	12 36 48.70	62 12 16.73	2.63	0.58	4.57		22.30(2.8)	12 36 48.62	62 12 15.7	20.97	...	2.238	2.437
CDFN48	12 37 09.53	62 14 35.73	2.51	0.61	4.15		<6.2						
CDFN49	12 36 57.15	62 14 08.71	2.00	0.50	4.02		28.20(5.2)	12 36 57.40	62 14 7.80	21.07	...	1.461	1.966

(This table is also available in a machine-readable form in the online journal.)

Table 2
SMA Sources

Name	SMA R.A. J2000.0 (deg)	SMA Decl. J2000.0 (deg)	SMA 860 μm (mJy)	SMA Ref.	VLA 1.4 GHz (mJy)	$z_{\rm spec}$	Redshift Ref.
(1)	(2)	(3)	(4)	(5)	(6)	(7)	(8)
GN20	189.29875	62.37000	23.9 ± 2.5	Iono et al. (2006)	87.5 ± 15.5	4.055	Daddi et al. (2009b)
CDFN1	188.98271	62.37761	17.0 ± 1.9	This paper	56.6 ± 7.6	...	...
850-6	189.37833	62.21639	14.9 ± 0.9	Barger et al. (2012)	126.0 ± 4.9	...	...
CDFN2	188.96399	62.36314	13.7 ± 2.8	This paper	51.9 ± 7.3	...	...
850-5	189.13937	62.23575	12.0 ± 1.4	Wang et al. (2007)	33.2 ± 5.6	4.042	Daddi et al. (2009a)
CDFN5	189.11333	62.10153	11.5 ± 0.7	This paper	34.2 ± 2.9	...	...
850-2	189.09212	62.27103	9.3 ± 1.4	Barger et al. (2012)	26.1 ± 6.1	...	...
850-1	189.21661	62.20716	7.8 ± 1.0	Cowie et al. (2009)	12.5 ± 2.4	5.183	Walter et al. (2012)
850-17	189.12018	62.17925	7.7 ± 0.9	Barger et al. (2012)	48.5 ± 9.4	...	...
850-3	189.07637	62.26411	7.2 ± 0.7	Barger et al. (2012)	163.6 ± 4.9	2.000	Pope et al. (2008)
CDFN15a	189.14693	62.32248	7.2 ± 1.7	This paper	...	...	...
CDFN10	189.13301	62.28742	7.1 ± 0.5	This paper	21.6 ± 2.5	...	...
CDFN18	189.42142	62.20567	7.1 ± 1.8	This paper	27.4 ± 2.7	...	...
850-9	189.28004	62.23564	7.1 ± 1.4	Barger et al. (2012)	25.9 ± 2.5	2.490	Swinbank et al. (2004)
CDFN15b	189.14975	62.32236	6.9 ± 1.7	This paper	...	...	...
850-36	189.29716	62.22533	6.7 ± 0.6	This paper	123.8 ± 5.4	1.995	Bothwell et al. (2010)
CDFN13	189.18367	62.32722	6.4 ± 1.1	This paper	25.4 ± 2.9	...	...
850-13c	189.30000	62.20341	5.3 ± 0.9	Wang et al. (2011)	33.0 ± 2.4	2.914	Chapman et al. (2005)
850-11b	189.18324	62.24742	5.3 ± 1.1	Wang et al. (2011)	30.8 ± 2.3	2.095	Reddy et al. (2006)
GN17	189.25667	62.19611	4.8 ± 0.6	This paper	95.2 ± 5.6	1.73	Pope et al. (2008)
850-16a	189.24390	62.15878	4.6 ± 0.6	This paper	27.5 ± 2.6	...	...
850-12	189.23300	62.20053	4.5 ± 0.8	Barger et al. (2012)	25.6 ± 6.4	2.737	Barger et al. (2008)
850-11a	189.19205	62.24683	4.2 ± 0.8	Wang et al. (2011)	101.0 ± 2.5	...	...
850-13b	189.30943	62.20225	4.1 ± 0.7	Wang et al. (2011)	25.5 ± 2.6	3.157	Barger et al. (2008)
850-15b	189.08875	62.28558	3.5 ± 0.7	Barger et al. (2012)	164.6 ± 5.0	1.992	Swinbank et al. (2004)
850-15a	189.08792	62.28600	3.4 ± 0.6	Barger et al. (2012)	44.9 ± 2.7	...	...
850-7	189.06712	62.25383	3.4 ± 0.6	Barger et al. (2012)	36.9 ± 2.6	2.578	Chapman et al. (2005)
850-13a	189.30847	62.19900	3.2 ± 0.9	Wang et al. (2011)	22.1 ± 2.5	...	...
850-16b	189.25125	62.15275	3.1 ± 0.6	This paper	297.2 ± 5.0	...	...

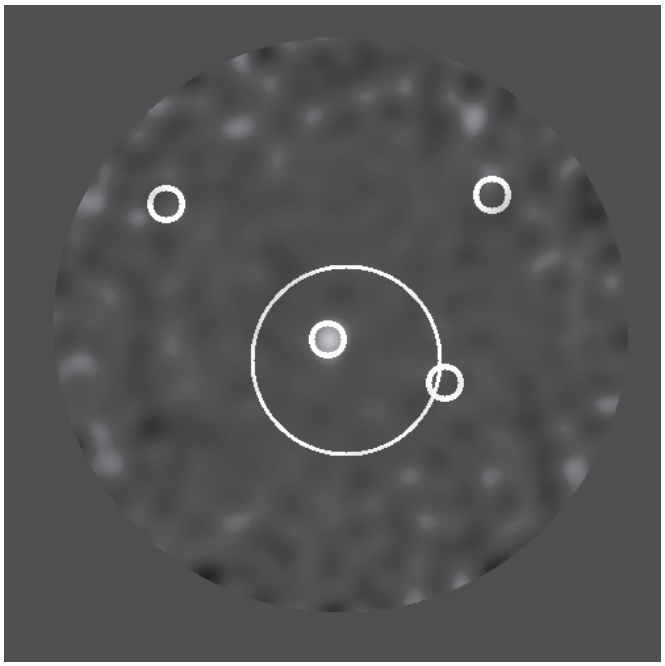

Figure 4. SMA image of CDFN8 with a measured 860 μm flux of 11.5 ± 0.7 mJy from the SMA and an 850 μm flux of 9.5 ± 2.3 mJy from SCUBA-2. The large circle shows the SCUBA-2 beam centered at the SCUBA-2 position. The small circles show the positions of 1.4 GHz sources in the field. The submillimeter source is a single unresolved source at the position of a 1.4 GHz source with a flux of 34.2 ± 2.9 μJy. None of the other three radio sources in the field have a significant submillimeter flux.

the image has a 1σ depth of 0.12 μJy. We measured 3″ diameter aperture K_s magnitudes corrected to total magnitudes at the positions of the radio sources using the K_s image. For sources brighter than $K_s = 19$, we used an isophotal magnitude computed using an aperture corresponding to 1% of the central surface brightness in the galaxy.

2.5. X-Ray Imaging

Alexander et al. (2003) presented the 2 Ms X-ray image of the CDF-N, which they aligned with the Richards (2000) radio image. Near the aim point, the X-ray data reach limiting fluxes of $f_{2-8\,\rm keV} \approx 1.4 \times 10^{-16}$ and $f_{0.5-2\,\rm keV} \approx 1.5 \times 10^{-17}$ erg cm^{-2} s^{-1}. We assume a conservative $L_X > 10^{42}$ erg s^{-1} as the threshold for a source to be classified as an X-ray AGN on energetic grounds (Zezas et al. 1998; Moran et al. 1999), and we assume $L_X > 10^{44}$ erg s^{-1} as the threshold for a source to be classified as an X-ray quasar.

2.6. Spectroscopic Redshifts

Many redshifts have been obtained of galaxies in the GOODS-N/CDF-N field using either the Low-Resolution Imaging Spectrograph (LRIS; Oke et al. 1995) on the Keck I 10 m telescope or the large-format DEep Imaging Multi-Object Spectrograph (DEIMOS; Faber et al. 2003) on the Keck II 10 m telescope. These include large magnitude-selected samples (Cohen et al. 2000; Cowie et al. 2004b; Wirth et al. 2004; Barger et al. 2008; Cooper et al. 2011) or targeted samples looking for interesting galaxy populations (Reddy et al. 2006; Chapman

et al. 2003, 2004a, 2005; Swinbank et al. 2004; Treu et al. 2005; Barger et al. 2002, 2003, 2005, 2007; Trouille et al. 2008). There are also a small number of CO redshifts that have been measured for SMGs in the region (Daddi et al. 2009a, 2009b; Bothwell et al. 2010; Walter et al. 2012).

We targeted new radio sources detected in the Owen14 catalog during DEIMOS runs in 2012 and 2013. We used the 600 line mm^{-1} grating, giving a resolution of 3.5 Å and a wavelength coverage of 5300 Å. The spectra were centered at an average wavelength of 7200 Å, although the exact wavelength range for each spectrum depends on the slit position. Each ~1 hr exposure was broken into three subsets, with the objects stepped along the slit by 1.″5 in each direction. Unidentified sources were continuously re-observed, giving maximum exposure times of up to 7 hr. We reduced the spectra in the same way as with previous LRIS spectra (Cowie et al. 1996). We only used spectra that could be identified confidently based on multiple emission and/or absorption lines. We identified a number of spectra using the doublet structure of the [O II] 3727 Å line, which is resolved in the spectra.

We also searched the infrared grism spectra obtained by PI: B. Weiner (*HST* Proposal ID 11600) using the G140 grism on the WFC3 camera on *HST*. We formed the spectra of 5709 galaxies with F140W < 24.5 and identified 607, mostly using the [O III]λ5007 doublet and Hβ or Hα. The galaxies primarily lie in the redshift interval $z = 0.8$–2.3. A full catalog will be given in future work. Of the identified sources, 107 are also radio sources; however, only 2 had not previously been identified from the optical spectra.

Of the 894 distinct radio sources in the full field 556 (62%) have secure spectroscopic redshifts either from the literature or from our targeted spectroscopy of the sample. In the GOODS-N region (here defined as the region that is well covered by the *HST* ACS observations of Giavalisco et al. 2004), 367 (67%) of 543 radio sources have spectroscopic redshifts. These spectroscopic identifications primarily come from UV/optical or NIR spectroscopy, but they also contain the small number of sources with CO spectroscopic redshifts.

2.7. Photometric Redshifts

Photometric redshifts can extend the spectroscopically identified sample and provide a check on the spectroscopic redshifts. Berta et al. (2011) compiled a multiwavelength catalog of sources in the GOODS-N field and computed photometric redshifts using the EAZY code of Brammer et al. (2008).

In comparing the spectroscopic and photometric redshifts, we only consider the spectroscopically identified radio sources in the spectroscopically well-covered area of the GOODS-N field having a photometric redshift quality flag $Q_z < 2$. We also eliminate photometric redshifts $z \leqslant 0.06$, which are invariably misidentifications of blue, higher redshift galaxies, and we restrict to galaxies with *HST* ACS F850LP < 26 (Giavalisco et al. 2004).

We show a comparison of the photometric and spectroscopic redshifts in Figure 5. Only 13 (red squares) of the 303 spectroscopic redshifts have strong disagreements with the corresponding photometric redshifts. This number is a strong function of the quality flag. For $Q_z = 1$, we find 5 strongly discrepant sources out of 243 radio sources, while for $Q_z = 3$, this rises to 19 out of 323. Thus, we adopt $Q_z < 2$ to maximize the number of included sources while not allowing too high of an error rate. We inspected all 13 discrepant sources individually to confirm both the galaxy identification and the spectral redshift

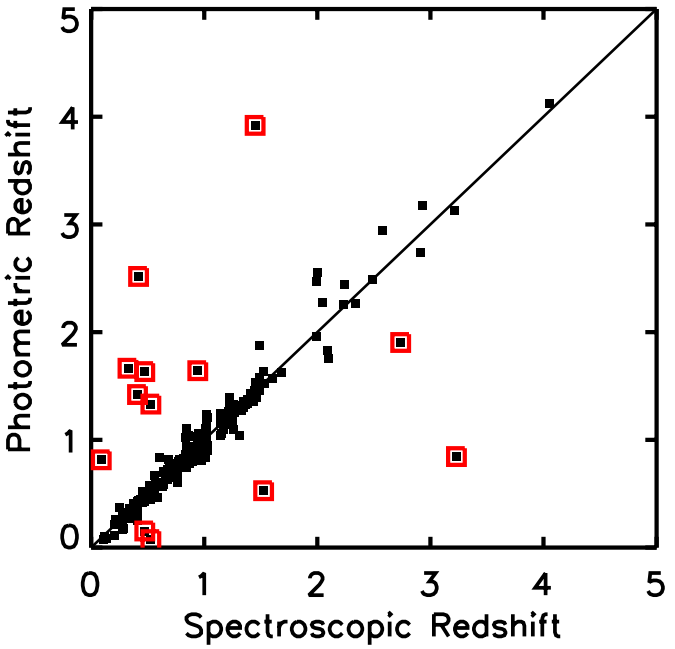

Figure 5. Comparison of spectroscopic redshifts with photometric redshifts from Berta et al. (2011). Only spectroscopically identified radio sources lying in the spectroscopically well-covered area of the GOODS-N field and having F850LP < 26, a photometric redshift quality flag of $Q_z < 2$, and $z > 0.06$ are shown. Of the 303 objects, 13 have serious discrepancies. These are marked with the red squares.

(A color version of this figure is available in the online journal.)

measurement. We concluded in all cases that the spectroscopic identification was reasonable. In some cases the photometric redshift may have been contaminated by blending of two distinct galaxies, while in other cases strong emission lines in the spectrum may have perturbed the photometric redshift estimate. However, there were some cases where we could not find an obvious explanation for the discrepancy.

Rafferty et al. (2011) determined photometric redshifts over the full field. Since these are based on more limited photometric information, we do not use them in our subsequent analysis. However, we include these in the photometric redshift column of Table 1 (marked with an (R)) where no photometric redshift is available from Berta et al. (2011).

2.8. Millimetric Redshifts

In Barger et al. (2012), we plotted the 1.4 GHz to 860 μm flux ratio versus $1 + z$ for the 16 SMGs in our SMA sample with spectroscopic redshifts. We found that the Barger et al. (2000) Arp 220-based model agreed reasonably well with a power-law fit over the observed spectroscopic redshift range. We therefore adopt this relation (Equation (5) of Barger et al. 2000) to measure millimetric redshifts (see also Carilli & Yun 1999) for the SMGs in the SMA sample of Table 2. In Figure 6, we compare these millimetric redshifts with the spectroscopic redshifts for the sources in the SMA sample with spectroscopic redshifts (see Table 2; black squares). The agreement is very good. For the SMGs without spectroscopic redshifts (blue diamonds), we use the millimetric redshifts on both axes. We mark X-ray AGNs with red small squares.

We searched a 3″ radius around each SMA position to find X-ray counterparts in the 2 Ms *Chandra* catalog of Alexander et al. (2003). Sources that contain AGNs are expected to follow the same relation as the non-AGNs, since both star-forming

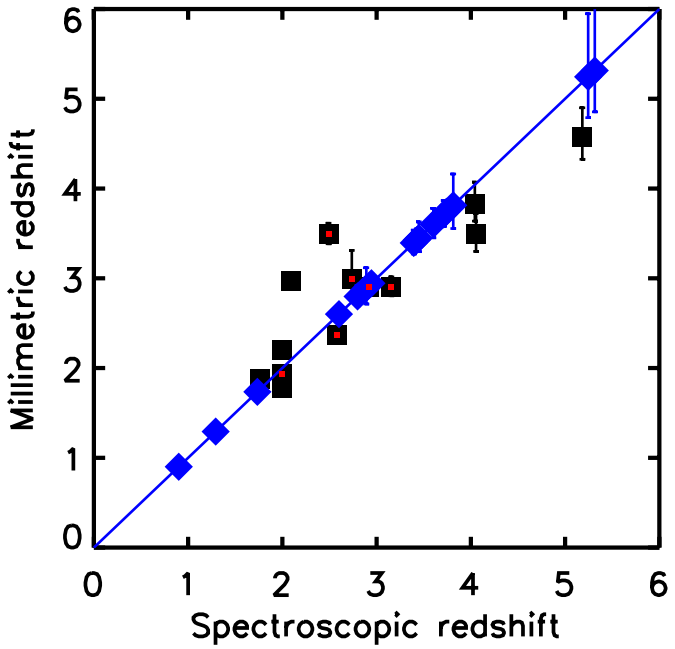

Figure 6. Millimetric redshifts estimated from the 1.4 GHz to 860 μm flux ratio using the Barger et al. (2000) Arp 220-based model vs. spectroscopic redshift. The SMGs in the SMA sample with spectroscopic redshifts are denoted by black squares. Those without spectroscopic redshifts are denoted by blue solid diamonds and are plotted at their millimetric redshifts on both axes. X-ray AGNs are marked with red small squares.

(A color version of this figure is available in the online journal.)

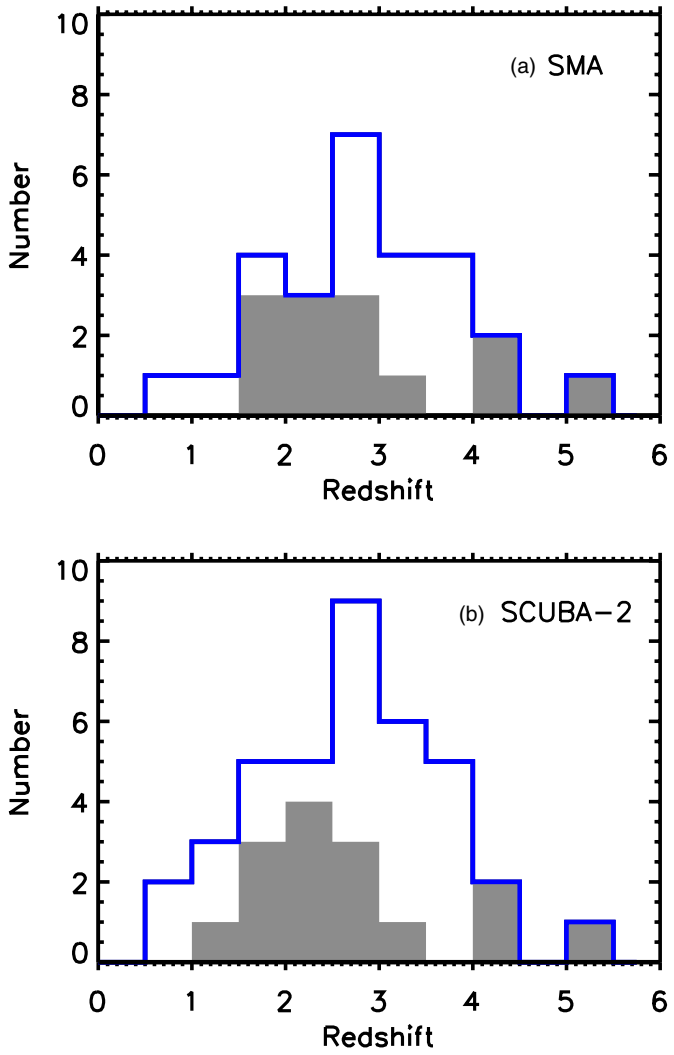

Figure 7. Histograms of the spectroscopic (gray shading) and millimetric (blue) redshifts for (a) the SMA sample and (b) the SCUBA-2 sample. In (a), the 27 SMA sources with radio counterparts in Table 2 are shown. The two omitted sources without counterparts (CDN15a and CDFN15b) are predicted to lie at $z > 5$ by the millimetric estimate. In (b), only sources with SMA identifications or single radio counterparts in the SCUBA-2 beam are shown (i.e., all but 8 of the 49 SCUBA-2 sources in Table 1).

(A color version of this figure is available in the online journal.)

galaxies and radio-quiet AGNs obey the same tight empirical correlation between non-thermal radio emission and thermal dust emission (e.g., Helou et al. 1985; Condon 1992). This is seen to be true from Figure 6, where we mark the X-ray AGNs with red squares. Only one of the five X-ray AGNs has only a millimetric redshift, which may be due to the fact that AGNs are easier to identify spectroscopically.

In Figure 7(a), we show the spectroscopic (gray shading) and millimetric (blue) redshift distributions for the SMA sample in histogram form. The millimetric redshifts predominantly fill in the $z \sim 2.5$–4 range. CDF15a and CDFN15b do not have radio counterparts, and are not shown in Figure 7(a), but the lower limit on the millimetric redshift based on the upper limit on the radio flux would place them at high redshift ($z > 5$). Unfortunately, it would be hard to model the selection effects for the SMA sample, given the diverse reasons for the observations.

All but eight of the sources in the SCUBA-2 sample have well-defined counterparts. We show the spectroscopic (gray shading) and millimetric (blue) redshift distributions in Figure 7(b). The spectroscopic redshifts range from $z = 1$ to just above $z = 5$, while the millimetric redshifts again predominantly fill in the $z \sim 2.5$–4 range. As in the SMA figure, the four sources with only radio upper limits, which are not shown in the figure, are likely to lie at higher redshifts.

3. REDSHIFT DISTRIBUTION OF THE RADIO SAMPLE

In Figure 8(a), we show how the spectroscopic completeness (gray shading) is very high for radio sources in the GOODS-N region (black histogram) with bright optical or NIR counterparts, and how the number of additional sources with secure photometric redshifts (green shading) is small. In the GOODS-N field, we have 367 spectroscopically identified radio sources, including 4 with CO redshifts (cyan shading). The photometric redshifts add only a further 30. The spectroscopic plus photometric redshift identifications are highly complete to $K_s \sim 21$, but nearly all have $K_s < 22.5$. In Figure 8(b), we show similar results for the radio sources in the full field (black histogram). We denote the spectroscopically identified sources with gray shading and the spectroscopically unidentified sources having clear submillimeter counterparts with blue shading. We can estimate millimetric redshifts for the latter sources, and CO redshifts may also be obtainable.

We see that there is an extended tail of radio sources with faint NIR counterparts ($K_s > 22.5$). This is the magnitude regime where many of the sources with millimetric redshifts lie and where all four of the sources with CO redshifts lie (all with $z \gtrsim 4$).

In each figure, we lumped the sources that are undetected in the K_s image into the faintest bin. These sources are also extremely optically faint: nearly all of the ones that lie in the GOODS-N region are undetected in the *HST* ACS images.

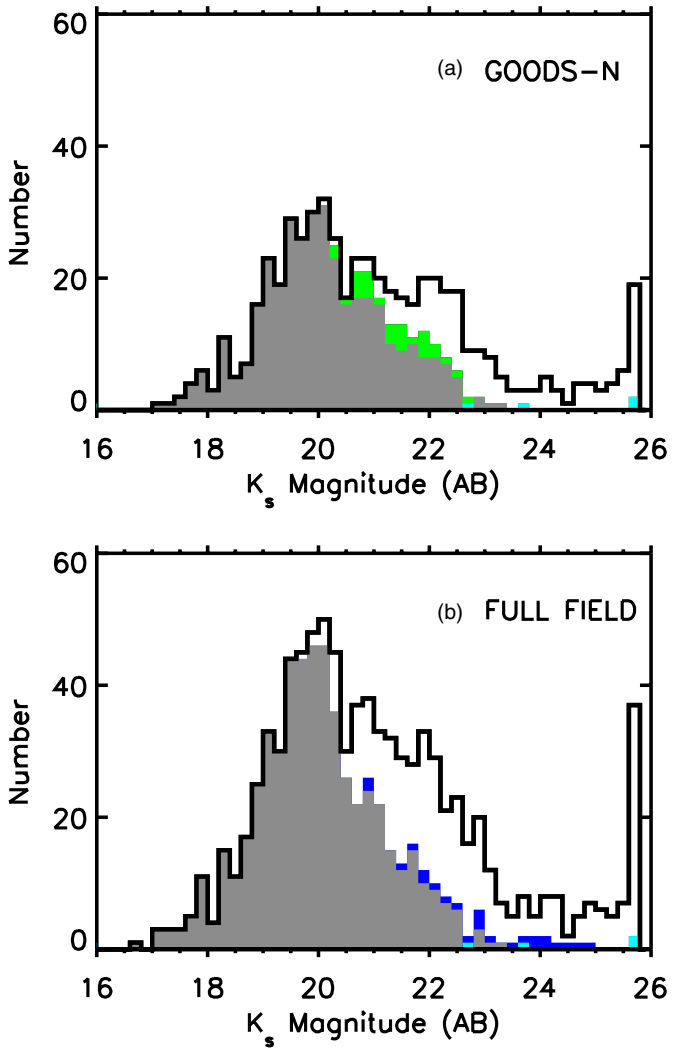

Figure 8. Histogram of the K_s magnitudes for the radio sources. The step size is 0.2 mag. Sources with K_s fainter than 25.7 are all put into the faintest bin. In (a), we show the sources in the GOODS-N region (gray shading—spectroscopic redshifts, cyan shading—CO redshifts, green shading—additional sources with photometric redshifts, no shading—sources without redshifts). In (b), we show the sources in the full field (gray shading—spectroscopic redshifts, cyan shading—CO redshifts, blue shading—additional sources having clear submillimeter counterparts for which we can measure millimetric redshifts, no shading—sources without redshifts).

(A color version of this figure is available in the online journal.)

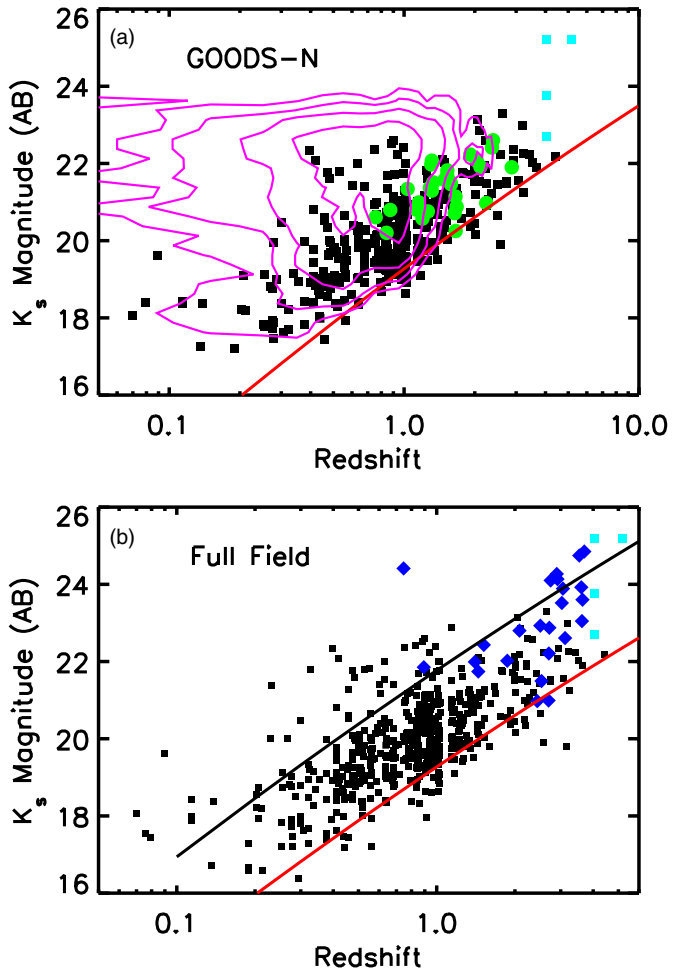

Figure 9. K_s magnitude vs. redshift for the radio sources. Sources undetected in K_s are shown at a nominal magnitude of 25.2. In (a), we show the radio sources in the GOODS-N region (black squares—spectroscopic redshifts, cyan squares—CO redshifts, green circles—photometric redshifts). The purple contours show the surface density of a K_s-selected field sample with spectroscopic redshifts in the GOODS-N region from Barger et al. (2008). The contours rise by multiplicative factors of two from the lowest contour with 1/40th of the peak surface density. In (b), we show the radio sources in the full field (black squares—spectroscopic redshifts, cyan squares—CO redshifts, blue diamonds—millimetric redshifts). The red line (also in (a)) shows the $K - z$ relation from Willott03. The black line shows the same relation with the K_s magnitude made fainter by 2.5 mag.

(A color version of this figure is available in the online journal.)

Unfortunately, such sources, which may lie at high redshifts, cannot be identified with either optical/NIR spectroscopy or photometry.

4. THE $K - z$ RELATION

Because of the potential for estimating redshifts for radio galaxies in the NIR-faint (likely high-redshift) tail using the $K - z$ relation, we now turn to examining that relation for our faint radio sample. In Figure 9(a), we show K_s magnitude versus spectroscopic (black squares), CO (cyan squares), or photometric (green circles) redshift for the radio sources in the GOODS-N region. By comparing with a K_s-selected field sample with spectroscopic redshifts in the GOODS-N region (Barger et al. 2008; purple contours show the surface density), we see that our radio sources are nearly all located in the most K_s luminous galaxies at all redshifts. Remarkably, the $K - z$ relation from Willott03 (red line; approximately converted from their K(Vega) to our K_s(AB) using a 1.9 mag offset) accurately traces the K_s luminous envelope of our sample over a wide range in K_s magnitude and redshift, indicating that some faint radio sources lie in the same galaxy mass hosts as powerful radio sources.

In Figure 9(b), we show K_s magnitude versus spectroscopic (black squares), CO (cyan squares), or millimetric (blue diamonds) redshift for the radio sources in the full field. The millimetric redshifts fill in the higher redshift part of the plot. We again show the Willott03 relation (red line), as well as the same relation with the K_s magnitude made fainter by 2.5 mag (black line). Nearly all of the radio sources lie in the band between the red and black lines. At low redshifts (out to $z \sim 1$), this could be a consequence of the rapid evolution in the maximum SFRs with increasing redshift, such that the radio selection is always

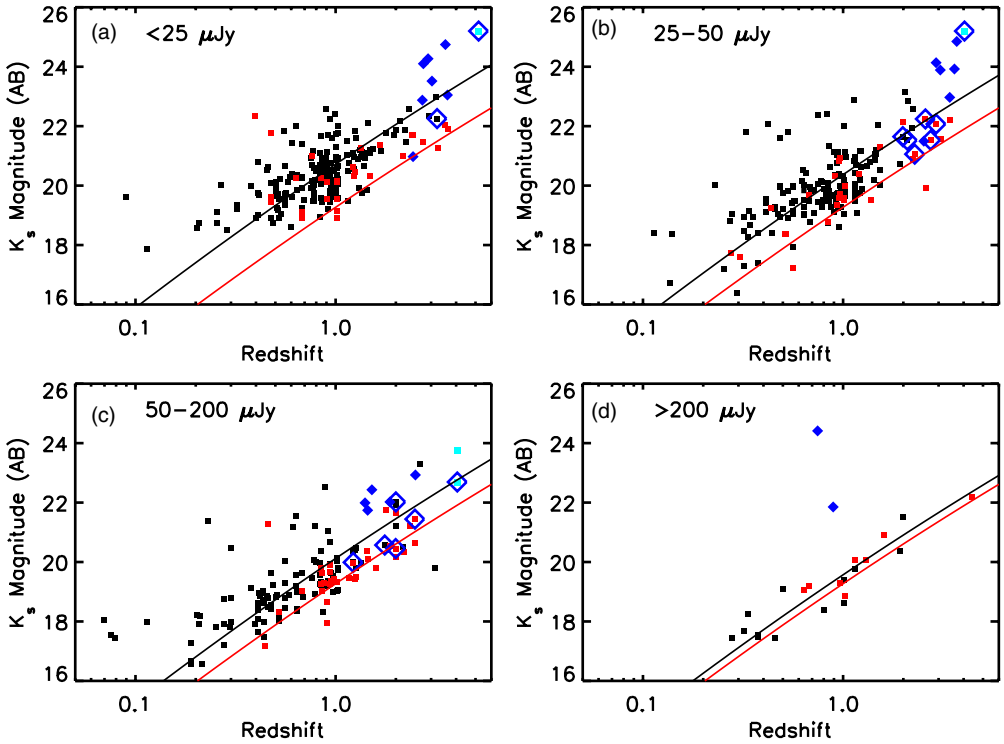

Figure 10. K_s magnitude vs. redshift in four 1.4 GHz flux intervals for radio sources in the GOODS-N: (a) <25 μJy, (b) 25–50 μJy, (c) 50–200 μJy, and >200 μJy. Sources undetected in K_s are shown at a nominal magnitude of 25.2. We show the radio sources in the full field (black squares—spectroscopic or photometric redshifts, cyan squares—CO redshifts, blue solid diamonds—millimetric redshifts). X-ray AGNs are marked with red squares. Sources with spectroscopic, photometric, or CO redshifts and SCUBA-2 detections are shown surrounded by blue large open diamonds. The red line shows the $K - z$ relation from Willott03. The black line shows the best-fit model using the shape of the Willott03 $K - z$ relation, but allowing ΔK_s in Equation (1) to vary.

(A color version of this figure is available in the online journal.)

dominated by the highest redshift and highest SFR galaxies (e.g., Condon 1989; Barger et al. 2007).

Eales et al. (1997) and Willott03 showed for the most powerful radio samples that the $K - z$ relation has a weak dependence on radio flux selection, with lower radio flux sources having fainter K-band magnitudes for the same redshift. More recently, Simpson et al. (2012) studied the $K - z$ relation for the $S_{1.4\,\mathrm{GHz}} > 100$ μJy sample in the Subaru/*XMM-Newton Deep Field*, which is about a factor of 1000 fainter than the faintest radio survey limit of Willott03, and found that at $z \gtrsim 1$, the sources were systematically fainter than the literature $K - z$ relations (Willott03; Brookes et al. 2008; Bryant et al. 2009).

Our $S_{1.4\,\mathrm{GHz}} > 11.5$ μJy sample shows a clear dependence of the $K - z$ relation on the radio flux selection. We illustrate this in Figure 10, where we show K_s magnitude versus spectroscopic or photometric (black squares), CO (cyan squares), or millimetric (blue solid diamonds) redshift in four radio flux intervals for the radio sources in the GOODS-N field. We mark X-ray AGNs with red squares and SCUBA-2 sources with spectroscopic, photometric, or CO redshifts with blue large open diamonds. In each radio interval, we adopt a $K - z$ relation having the Willott03 shape (see their Equation (2)),

$$K_s = \Delta K_s + 4.53 \log_{10} z - 0.31 (\log_{10} z)^2. \quad (1)$$

We obtain least-squares fits to the data by adjusting the K_s offset (ΔK_s). In each panel, we show our fits in black and the Willott03 relation ($\Delta K_s = 17.37$) in red. Remarkably, the observed dependence on radio flux appears to hold for all sources, whether they are star-formation-dominated or AGN-dominated. However, by $z \gtrsim 3$, the SCUBA-2 sources (blue solid or open diamonds) appear fainter than expected, as was also observed by Dunlop (2002) and Serjeant et al. (2003b) for SCUBA sources.

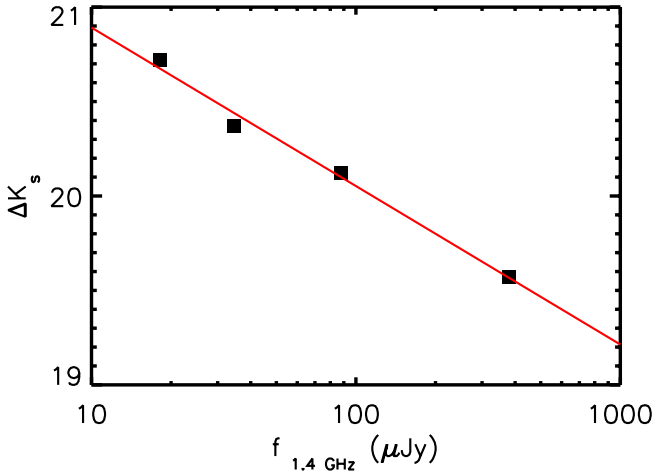

Figure 11. Black squares show the ΔK_s values (20.72, 20.37, 20.12, 19.57) determined in the radio flux intervals of Figure 10 vs. the mean radio fluxes in the intervals (18.1, 34.7, 87.6, and 308.9 μJy). The red line shows the least-squares fit of ΔK_s vs. $\log_{10} f_{1.4\,\mathrm{GHz}}$ (Equation (2)).

(A color version of this figure is available in the online journal.)

In Figure 11, we plot the ΔK_s values found from our fits versus the mean radio fluxes for each interval. These data points are well fit by the functional form

$$\Delta K_s = 21.73 - 0.84 \log_{10} f_{1.4\,\mathrm{GHz}}, \quad (2)$$

which we show in the figure with the red line. Here $f_{1.4\,\mathrm{GHz}}$ is in μJy.

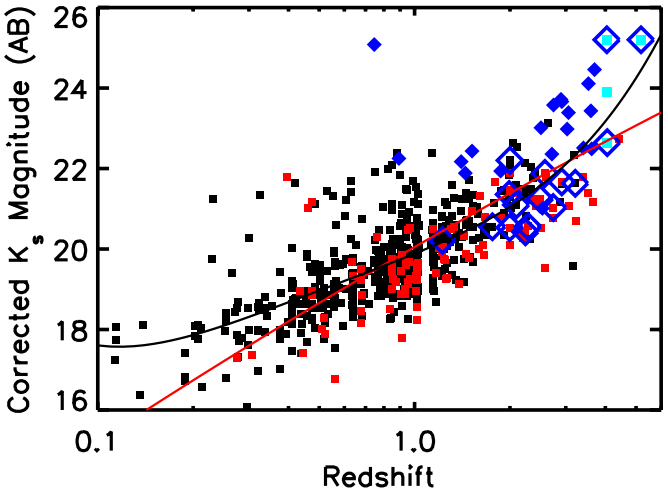

Figure 12. K_s magnitude corrected to $K_{\rm corr}$ using Equation (3) for the radio sources in the GOODS-N vs. redshift (black squares—spectroscopic or photometric redshifts, cyan squares—CO redshifts, blue solid diamonds—millimetric redshifts). X-ray AGNs are marked with red squares. Sources with spectroscopic, CO, or photometric redshifts and SCUBA-2 detections are shown surrounded by blue large open diamonds. The curve from Equations (1) and (2) for $f_{1.4\,\rm GHz} = 100\ \mu$Jy is shown in red. The fourth order polynomial fit to the data from Equation (4) is shown in black.

(A color version of this figure is available in the online journal.)

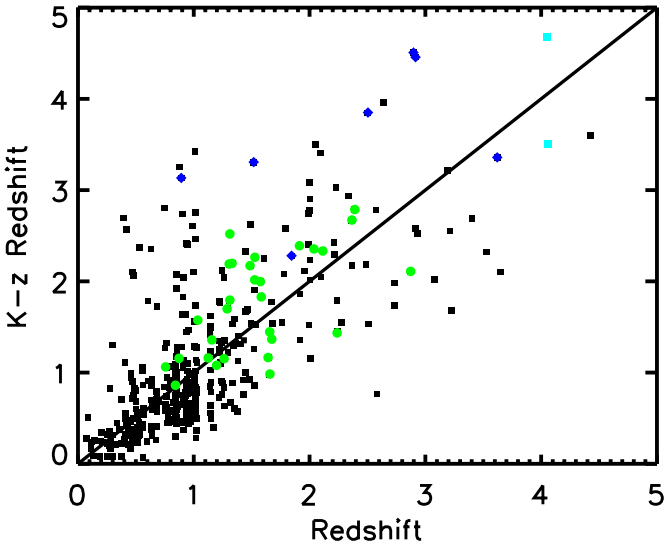

Figure 13. Redshift estimated from the $K-z$ relation (Equations (3) and (4)) vs. spectroscopic (black squares), CO (cyan squares), photometric (green circles), or millimetric (blue diamonds) redshift for the radio sources in the GOODS-N field with such information.

(A color version of this figure is available in the online journal.)

This relation also extrapolates approximately to fit the highest radio flux samples of previous work. An exact comparison is difficult, however, because those samples are chosen at different radio frequencies, and we cannot precisely convert the NIR photometry. Willott03 found a 0.55 mag difference in the mean ΔK for the 3CRR and 7C samples. Since the 7C sample is 20 times fainter, that would correspond to a slope of 0.42 in Equation (2), suggesting that brighter radio sources may follow a shallower relation.

From Equation (2), we can see that the observed K_s-band flux depends on the observed 1.4 GHz flux to the power of 0.34. This is a very weak dependence, which means that for a large range in radio flux, there is only a small range in host galaxy K_s-band flux. Thus, for our sample, with $f_{1.4\,\rm GHz}$ ranging from 11.5 to 5276 μJy, the range in f_{K_s} is only 7.8. The corresponding range in K_s is 2.2 mag, consistent with the range seen in Figure 9(a).

We may use the dependence of the ΔK_s values on $f_{1.4\,\rm GHz}$ to tighten the relation between the K_s magnitude and the redshift for the radio sources. We define a corrected K_s magnitude, $K_{\rm corr}$, as

$$K_{\rm corr} \equiv K_s + 0.84 \log_{10}(f_{1.4\,\rm GHz}/100\,\mu{\rm Jy}) \quad (3)$$

to move all of the sources to the track followed by 100 μJy sources. In Figure 12, we plot $K_{\rm corr}$ versus redshift.

We made a fourth order polynomial fit to the data in Figure 12,

$$K_{\rm corr} = 19.88 + 3.20 \log_{10} z + 1.13(\log_{10} z)^2 + 2.79(\log_{10} z)^3 + 2.58(\log_{10} z)^4. \quad (4)$$

Above $K_s = 22$, our spectroscopic and photometric identifications in the GOODS-N are extremely incomplete, with the spectroscopic identifications likely biased toward star-forming galaxies and AGNs, so this turn up may not be representative of the full radio population. However, we can use Equation (4) to obtain rough redshift estimates for the radio sources. We show these in Figure 13 plotted versus spectroscopic, photometric, millimetric, or CO redshift for the radio sources in the GOODS-N field with such information.

5. RADIO POWER AND SUBMILLIMETER FLUX

Locally, most radio sources more powerful than $P_{1.4\,\rm GHz} = 10^{30}$ erg s^{-1} Hz^{-1} are found to be associated with AGN activity (e.g., Condon 1989; Sadler et al. 2002; Best & Heckman 2012). However, as we move to higher redshifts where dusty galaxies with high SFRs become more common (e.g., Cowie et al. 2004a), it is possible that some fraction of the $P_{1.4\,\rm GHz} > 10^{30}$ erg s^{-1} Hz^{-1} radio sources are dominated by star formation. Indeed, as we discussed in the Introduction, all $z \gtrsim 4$ radio galaxies may have high SFRs ($\gtrsim$1000 $M_\odot$ yr^{-1}) based on modeling of the $K-z$ relation (Rocca-Volmerange et al. 2004), and such SFRs have been observed (e.g., Dunlop et al. 1994; Ivison et al. 1998; Archibald et al. 2001; Reuland et al. 2004). Thus, our radio sample should provide a powerful way of finding such sources. However, separating the contributions to the radio emission from star formation and AGN activity is not straightforward.

We compute the rest-frame radio powers for the radio sources in the full field assuming $S_\nu \propto \nu^\alpha$ and a radio spectral index of $\alpha = -0.8$ (Condon 1992; Ibar et al. 2010) using

$$P_{1.4\,\rm GHz} = 4\pi {d_L}^2 S_{1.4\,\rm GHz} 10^{-29} (1+z)^{\alpha-1}\ {\rm erg\ s^{-1}\ Hz^{-1}}. \quad (5)$$

Here d_L is the luminosity distance (cm) and $S_{1.4\,\rm GHz}$ is the 1.4 GHz flux density (μJy). In Figure 14, we show these radio powers versus redshift for the sources with spectroscopic (including CO; black squares) or photometric (green circles) redshifts. For the remaining sources (red plus signs), we use the redshifts estimated from the $K_s - z$ relation (Equations (3) and (4)). We also plot the radio catalog limit of 11.5 μJy (5σ; blue dotted curve) and the radio powers of a luminous infrared galaxy (LIRG; $L_{\rm FIR} > 10^{11}\ L_\odot$; dashed horizontal line) and an ultraluminous infrared galaxy (ULIRG; $L_{\rm FIR} > 10^{12}\ L_\odot$; solid horizontal line), which we calculated by assuming that the FIR–radio correlation holds. At $z \gtrsim 3$, our radio observations are only sensitive to star-forming galaxies brighter than the ULIRG limit.

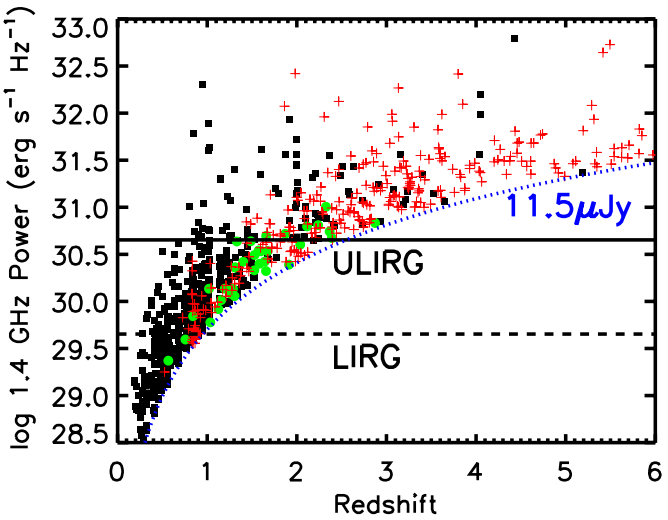

Figure 14. Radio power vs. redshift for the radio sources in the full field with spectroscopic or CO redshifts (black squares) or photometric redshifts (green circles). The remaining sources are shown at the redshifts that would be predicted from the $K-z$ relation (red plus signs; Equations (3) and (4)). The blue dotted curve shows the radio power corresponding to the 1.4 GHz catalog limit of 11.5 μJy (5σ). The dashed and solid horizontal lines show the radio powers that correspond to the definitions of a LIRG and a ULIRG, respectively, which we calculated by assuming that the galaxies are star formers and that the FIR–radio correlation holds.

(A color version of this figure is available in the online journal.)

5.1. High Radio Power

Our primary interest in this paper is to determine whether there is a turn-down in the SFR distribution function at high redshifts. Thus, we now turn our attention to the high radio power sources in our sample, which we define as having $P_{1.4\,\mathrm{GHz}} \geqslant 10^{31}$ erg s^{-1} Hz^{-1}.

In Figures 15(a) and (b), we show blow ups of Figure 14 to focus on the high radio power sources with secure redshifts. We have 51 (50 are spectroscopic or CO, and 1 is photometric), 39 of which are at $z > 1.5$. Most of the spectroscopically unidentified sources are faint in K_s and hence are likely to lie at high redshifts based on the $K-z$ relation (see Figure 14). For example, if we include our $K-z$ estimated redshifts, then the ratio of secure to total $z > 1.5$ sources would be 39/226, which would mean we have secure identifications for $\lesssim$1/5 of the high-redshift, high radio power sources.

In Figure 15(a), we distinguish sources where the X-ray data show them to be X-ray AGNs (red squares) or X-ray quasars (red large squares). We use green squares to distinguish sources that are likely to be elliptical galaxies, as determined by their having rest-frame EW([O II] λ3727) < 10 Å. The latter distinction can only be made from the optical spectra for galaxies at $z < 1.5$ (the dotted vertical line shows $z = 1.5$). We show with the blue dotted curve the radio limit of 11.5 μJy (5σ).

In Figure 15(b), we mark radio sources with 850 μm counterparts detected above the 4σ level (blue circles). (If there is no SMA measurement, then we only mark the source if there is a single radio counterpart within the SCUBA-2 beam.) We show with the blue dashed curve the 850 μm limit of 4 mJy (4σ) for the higher sensitivity region of the SCUBA-2 map (see Figure 2) converted to a radio power assuming an Arp 220 SED. Thus, over most of our SCUBA-2 map we would not expect to be able to detect a source having a radio power much less than our high radio power source definition.

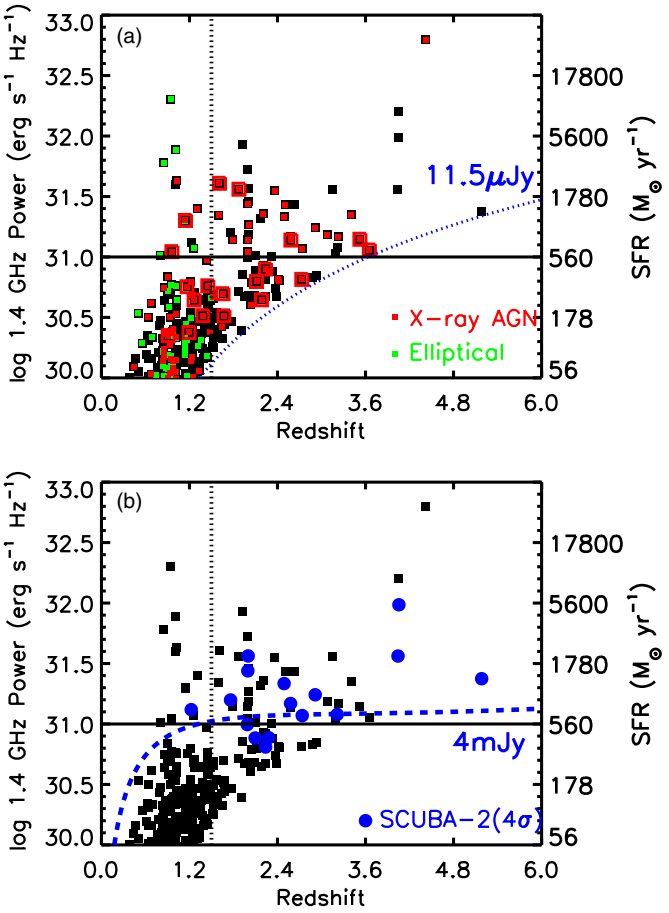

Figure 15. Radio power vs. redshift for the $P_{1.4\,\mathrm{GHz}} > 10^{30}$ erg s^{-1} Hz^{-1} radio sources in the full field with spectroscopic, CO, or photometric redshifts (black squares). The solid horizontal line shows our high radio power dividing line of $P_{1.4\,\mathrm{GHz}} = 10^{31}$ erg s^{-1} Hz^{-1}. (a) Green squares show radio sources with measured rest-frame EW([O II] λ3727) < 10 Å; only $z < 1.5$ sources can be classified as elliptical galaxies this way. X-ray AGNs are marked with red squares, and X-ray quasars are marked with red large squares. The blue dotted curve shows the radio power corresponding to the 1.4 GHz catalog limit of 11.5 μJy (5σ). (b) Blue circles show single radio sources with $>4\sigma$ 850 μm counterparts. The blue dashed curve shows the 850 μm limit of 4 mJy (4σ) for the higher sensitivity region of the SCUBA-2 map (see Figure 2) converted to a radio power assuming an Arp 220 SED. The right-hand y-axes show the SFRs that would correspond to the radio powers if the sources are powered by star formation (see Section 5.4).

(A color version of this figure is available in the online journal.)

Nearly all of the high radio power sources at $z < 1.5$ are X-ray quasars or elliptical galaxies (see Figure 15(a)), both of which are likely to be AGN-powered (Condon 1989; Sadler et al. 1989; Condon et al. 2013 and references therein). Of the two remaining sources, one is a SCUBA-2 source, and the other is likely to be AGN-powered, since it would be easily detectable with SCUBA-2 if it were dominated by star formation (see Figure 15(b)).

In contrast, at high redshifts ($z > 1.5$), a substantial fraction of the high radio power sources are detected at $>4\sigma$ in the submillimeter data. In Section 5.4, we use the (albeit limited) available data to show that high radio power sources detected with SCUBA-2 are primarily extended and dominated by star formation rather than spatially compact and dominated by AGN activity. Thus, our detection at 850 μm of 15 of the 41 high radio power sources at $z > 1.5$ suggests that 37% are star formers.

However, there are strong selection effects in the spectroscopic identifications of the radio sources at high redshifts, both

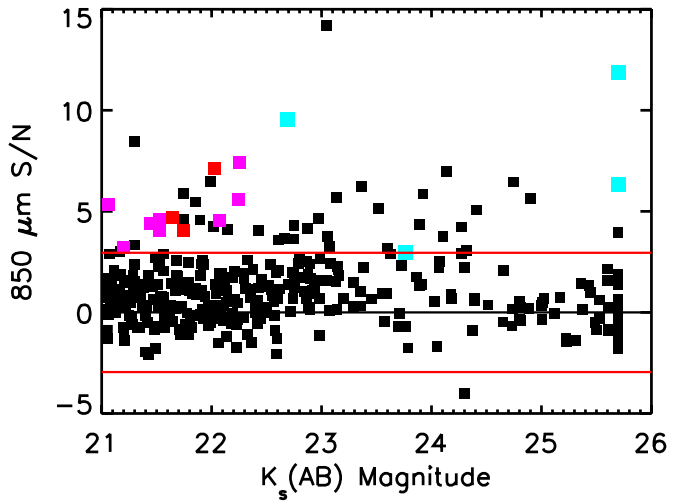

Figure 16. 850 μm signal-to-noise ratio vs. K_s magnitude for the $K_s > 21$ radio sources in the region of the SCUBA-2 image where the rms 850 μm noise is less than 1 mJy. The red horizontal lines mark the 3σ positive and negative noise levels. The red (pink) squares show galaxies with spectroscopic or photometric redshifts $z = 1$–2 ($z = 2$–4). The cyan squares show galaxies with CO redshifts (these are all at $z > 4$; see Figure 9).

(A color version of this figure is available in the online journal.)

in the targeting (e.g., by investing long integration times on the submillimeter detected galaxies through multiple masks or by obtaining CO redshifts) and in the ease of making the identifications (e.g., by seeing strong emission line features). Indeed, since "red and dead" galaxies would be hard to identify spectroscopically at high redshifts and hence do not appear on Figure 15, we may expect that our star-forming fraction is overestimated.

We test the impact of our spectroscopic incompleteness on our estimated star-forming fraction using the $K_s > 21$ high radio power sources. At $K_s \leqslant 21$, the combined spectroscopic and photometric redshifts provide an essentially complete identification of the radio sample in the GOODS-N region (see Figure 8(a)). It is only above this magnitude where the identifications become substantially incomplete.

In Figure 16, we show 850 μm S/N versus K_s magnitude for the $K_s > 21$ high radio power sample in the region of the SCUBA-2 image where the rms 850 μm noise is <1 mJy. Based on the $K - z$ relation, the unidentified $K_s > 21$ sources are estimated to lie at high redshifts. Consistent with this are the high redshifts of the sources with spectroscopic, CO, or photometric identifications, which we mark on the plot using red ($z = 1$–2), pink ($z = 2$–4), and cyan squares ($z > 4$). Thus, we can roughly compare with our previous estimate made for the secure $z > 1.5$ sources. We find that 29 of the 179 (16%) sources in the figure are detected above the 3σ level at 850 μm, and 23 of 179 (13%) are detected above the 4σ level. This result is insensitive to choosing a fainter K_s magnitude threshold.

5.2. Radio-power-based Star Formation Rates

If, as we shall argue in Section 5.4, the submillimeter-detected radio galaxies are primarily star-formation-dominated, then we can calculate the SFRs for the individual galaxies from their radio powers. However, in order to do so, we need to assume that the FIR–radio correlation is roughly invariant to $z \sim 6$. Barger et al. (2012) showed this to be true at $z = 2$–4.2 for luminous SMGs, but here we assume that the FIR–radio correlation extends to our highest sensitivity 850 μm flux threshold of 2 mJy (4σ), which is about a factor of two lower than the fluxes of the five SMGs in the Barger et al. (2012) clean SMA sample (see their Section 5) with well-determined SEDs and measured FIR luminosities (hereafter, the five SMGs).

We convert radio power to SFR using the FIR–radio correlation (Helou et al. 1985; Condon et al. 1991), parameterized by the quantity q,

$$q = \log\left(\frac{L_{\rm FIR(8-1000\,\mu m)}}{3.75\times10^{12}\ {\rm erg\ s^{-1}}}\right) - \log\left(\frac{P_{\rm 1.4\,GHz}}{\rm erg\ s^{-1}\ Hz^{-1}}\right), \quad (6)$$

and the Kennicutt (1998) relation between $L_{\rm FIR(8-1000\,\mu m)}$ and SFR. This gives

$$\log {\rm SFR}(M_\odot\ {\rm yr^{-1}}) = \log P_{\rm 1.4\,GHz}({\rm erg\ Hz^{-1}}) - A. \quad (7)$$

To determine the normalization constant, A, we use the $\langle q\rangle = 2.51$ value obtained by Barger et al. (2012) from the five SMGs. We find $A = 28.25$, a value which is almost identical to that determined by Bell (2003; $A = 28.26$) and about a factor of two lower than that determined by Condon (1992) based on the Milky Way. Barger et al. (2012) followed Cowie et al. (2011) in using an intermediate normalization of $A = 28.1$, which is a factor of 1.4 higher than the present value. However, here, in order to be consistent with our submillimeter determinations of the SFRs, we stay with $A = 28.25$. The factor of two range between the Bell and Condon determinations is probably a reasonable measure of the systematic uncertainty in the SFR–radio power relation.

The SFRs that we obtain from Equation (7) are for a −1.35 power-law Salpeter (1955) initial mass function (IMF) extending from 0.1–100 $M_\odot$. (This assumption is built into our adopted value of the normalization constant A through our use of the Kennicutt 1998 relation, which is calculated for that IMF.) The Salpeter IMF only differs significantly from the current best IMFs of Kroupa (2001) and Chabrier (2003) below 1 $M_\odot$. One can roughly convert the Salpeter IMF SFRs into Chabrier IMF SFRs by dividing by 1.39 and the Salpeter IMF SFRs into Kroupa IMF SFRs by dividing by 1.31.

On the right-hand y-axes of Figure 15, we show the SFR scale corresponding to the radio power scale for the radio star formers. Our high radio power source definition corresponds to an SFR of 560 $M_\odot$ yr^{-1} for a star formation dominated radio source. The submillimeter detected sources are seen to have SFRs up to ~6000 $M_\odot$ yr^{-1}.

At very high redshifts, the relation between SFR and radio power, and presumably also the FIR–radio correlation, must begin to break down, particularly for less luminous galaxies, because the Compton cooling of the relativistic electrons on the cosmic microwave background (CMB), which increases rapidly with increasing redshift, will begin to dominate over synchrotron losses (e.g., Condon 1992). This will decrease the radio power for a given SFR. The cross-over point will occur when the energy density in the CMB becomes comparable to the magnetic field energy density in the galaxy.

We emphasize that such additional sources of cooling would cause us to underestimate the SFRs based on the observed radio power. However, for the ULIRGs of the present sample, where the magnetic field and relativistic energy density are expected to be extremely high, this breakdown of the FIR–radio correlation may not occur over the $z < 6$ redshift range that we are considering.

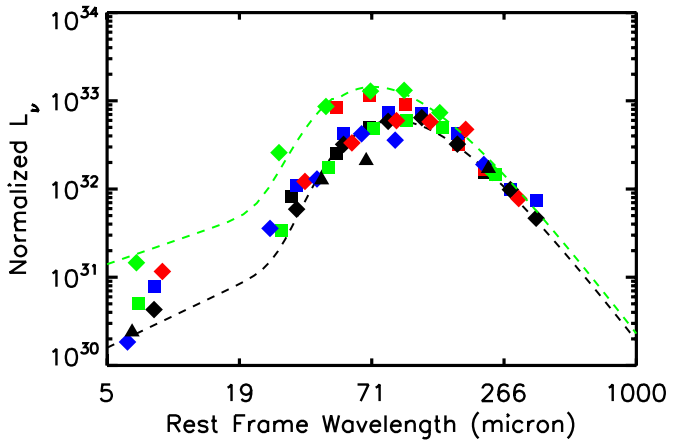

Figure 17. SEDs for the nine isolated SMGs with spectroscopic or CO redshifts between $z = 1.5$ and 5 and substantial coverage from the *Herschel* satellite. We show rest-frame L_ν divided by observed-frame SMA flux. The SEDs are very similar for seven of the sources but higher for the remaining two. The sources shown are CDFN3 (black squares), CDFN11 (red squares), CDFN13 (blue squares), CDFN14 (green squares), CDFN16 (black diamonds), CDFN22 (red diamonds), CDFN27 (blue diamonds), CDFN29 (green diamonds), and CDFN37 (black triangles). The two curves show the combined gray body and power-law fits to the SEDs of CDFN3 (black) and CDFN29 (green).

(A color version of this figure is available in the online journal.)

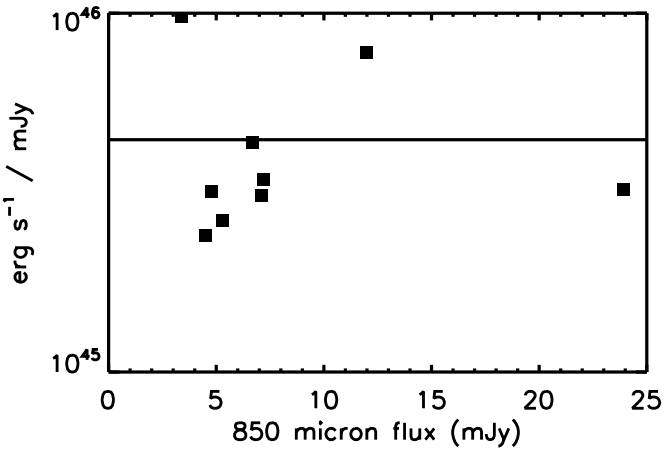

Figure 18. Ratio of measured $L_{\rm FIR(8-1000\,\mu m)}$ to observed-frame SMA flux vs. observed-frame SMA flux for the nine isolated SMGs with spectroscopic or CO redshifts above 1.5 and substantial coverage from the *Herschel* satellite. The solid line shows the mean conversion of 4.44×10^{45} erg s^{-1} mJy^{-1}.

5.3. Submillimeter-flux-based Star Formation Rates

For sources with spectroscopic or photometric redshifts, we can compute the SFR directly from the observed-frame 850 μm flux using the Kennicutt (1998) relation between $L_{\rm FIR(8-1000\,\mu m)}$ luminosity and SFR, if we assume a spectral shape, such as Arp 220. As is well known, this relation is almost redshift-independent for sources above $z = 1.5$ (Blain & Longair 1993; see the blue dashed curve in Figure 15(b)). For an Arp 220 shape obtained from the fits of Klaas et al. (1997) over the 8–1000 μm range, the relation is $\rm SFR_{850\,\mu m} = 180 \times S_{850\,\mu m}$, where $\rm SFR_{850\,\mu m}$ is in $M_\odot$ yr^{-1}, and $S_{850\,\mu m}$ is in mJy.

We may directly measure the conversion for the nine SMGs that are spatially isolated based on the SMA and 24 μm images, have spectroscopic or CO redshifts greater than 1.5, and are covered by the *Herschel* data. (The five SMGs of Barger et al. 2012 are a subset of this sample.) We first compiled the fluxes in the 24, 70, 100, 160, 250, 350, 500, 860, and 1100 μm bands from Magnelli et al. (2012, 2013), Barger et al. (2012), and Perera et al. (2008). In Figure 17, we show the rest-frame L_ν divided by the observed-frame SMA flux for these nine sources. Hereafter, we will say 850 μm everywhere instead of alternating between 850 μm (SCUBA-2) and 860 μm (SMA), since, within the uncertainties, the differences are not important.

For each source we fitted both a gray body and, below a rest-frame wavelength of 50 μm, a power law (see, e.g., Casey 2012 for a discussion of the fitting procedures). We show two sample fits in Figure 17. In Figure 18, we show the $L_{\rm FIR(8-1000\,\mu m)}$ to observed-frame 850 μm flux ratios that we determined from the fits versus the 850 μm flux. Converting these luminosities to SFRs using the Kennicutt (1998) formula, we find a mean conversion at $z > 1.5$ of

$$\rm SFR_{850\,\mu m} = 200 \times S_{850\,\mu m}, \quad (8)$$

with a multiplicative range over the individual values of just over two in each direction about the mean. (Seven of the sources have similar conversions, while two of the sources have higher conversions.) We adopt this value, which is quite close to that inferred from the Arp 220 shape, as our conversion factor. We will assume that the multiplicative range of two is the systematic error in the individual SFRs determined from the submillimeter fluxes based on the variations in their SEDs.

We also computed the mean fluxes for the isolated sample based on our own direct measurements in the GOODS-*Herschel* images (DR1 release; Elbaz et al. 2011). We measured the fluxes using a matched filter equal to the PSF of the image centered at the radio position. We compared the SFR conversion for the fainter sources at 850 μm (2–5 mJy) with that for the brighter (>5 mJy) sources. For both samples, we computed the mean luminosity normalized to the observed-frame 850 μm flux at the mean rest-frame wavelength of the sample. We only included sources lying within regions of the 100 μm image where the exposure time was greater than 25% of the maximum exposure time. We computed the background correction and the 68% confidence limits by constructing 100 equivalent samples with the same redshift distribution but randomized positions.

In Figure 19(a), we show the results for the spectroscopic sample only, and in Figure 19(b), we show the results for a much larger sample that uses millimetric redshifts when we do not have spectroscopic redshifts. The 2–5 mJy sample conversion is 2% higher than the >5 mJy sample conversion if we use the spectroscopic sample, and it is 25% lower than the >5 mJy sample conversion if we use the spectroscopic plus millimetric redshift sample. However, in both cases, the SEDs are consistent within the errors. (Note that because the noise is due to confusion, the errors are correlated between bands.) We therefore conclude that the SFR conversion is not strongly dependent on flux over the observed flux range. A similar test shows no evolution in the SFR conversion as a function of redshift.

We can only obtain independent estimates of the SFRs from the radio power and the submillimeter flux where we have spectroscopic, CO, or photometric redshifts. Where we only have millimetric redshifts, the SFRs obtained from the radio power will agree with those from the submillmeter fluxes by construction, since we are using a consistent assumption about the FIR SED.

In Figure 20, we compare the SFRs derived from the two methods for sources with spectroscopic, CO, or photometric redshifts $z > 1.5$. The SFRs derived are in good agreement, though the submillimeter-derived SFRs are about 5% higher, on

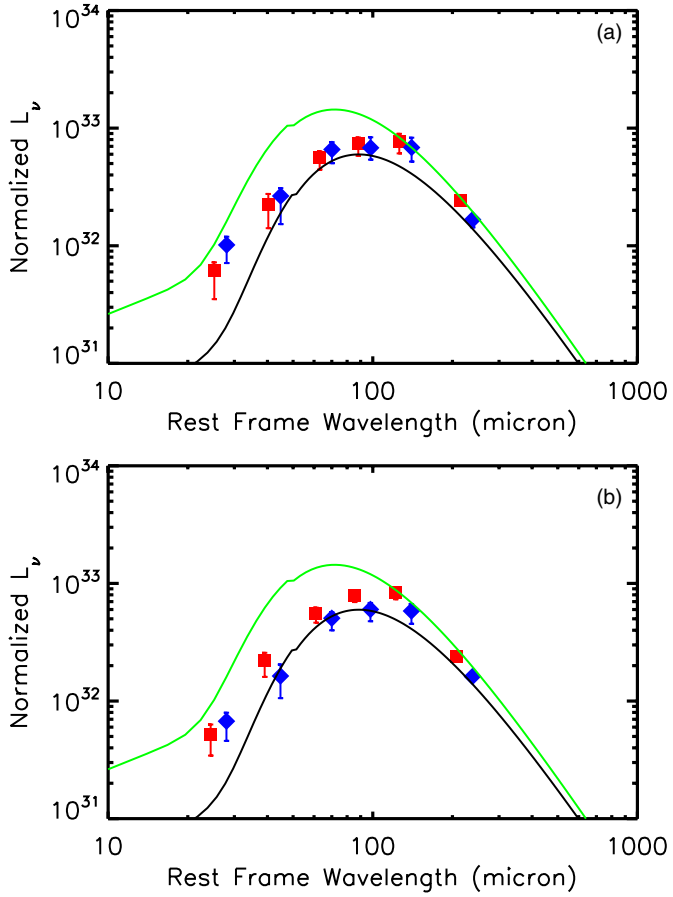

Figure 19. Mean value of L_ν divided by observed-frame 850 μm flux in each of the *Herschel* bands from 100 to 500 μm and in the SCUBA-2 850 μm band vs. the mean rest-frame wavelength of the sample. The blue diamonds (red squares) show the values for isolated sources with radio source identifications and 850 μm fluxes between 2 and 5 mJy (>5 mJy). (a) Sources with spectroscopic redshifts. (b) Sources with spectroscopic redshifts or with millimetric redshifts when there is no spectroscopic identification. The latter includes 12 sources in the high flux range and 16 sources in the low flux range. The two solid curves show the combined gray body and power-law fits to the SEDs of CDFN3 (black) and CDFN29 (green) from Figure 17, which give the range of the individual fits.

(A color version of this figure is available in the online journal.)

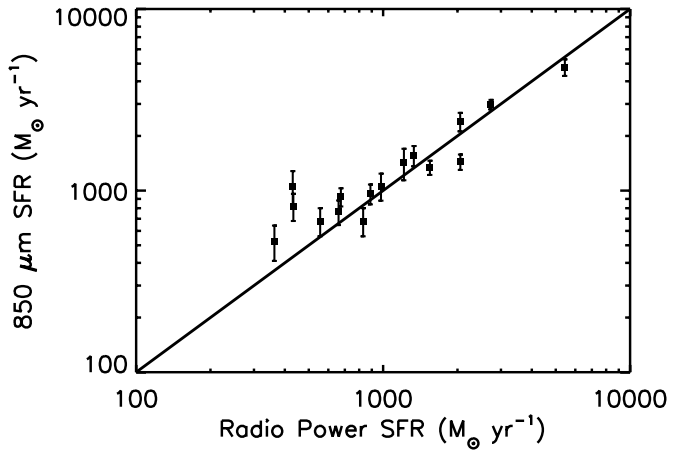

Figure 20. Comparison of the SFRs derived from the radio power with those derived from the 850 μm flux for the sources with spectroscopic, photometric, or CO redshifts $z > 1.5$. The submillimeter derived SFRs are about 5% higher, on average, than the radio derived SFRs.

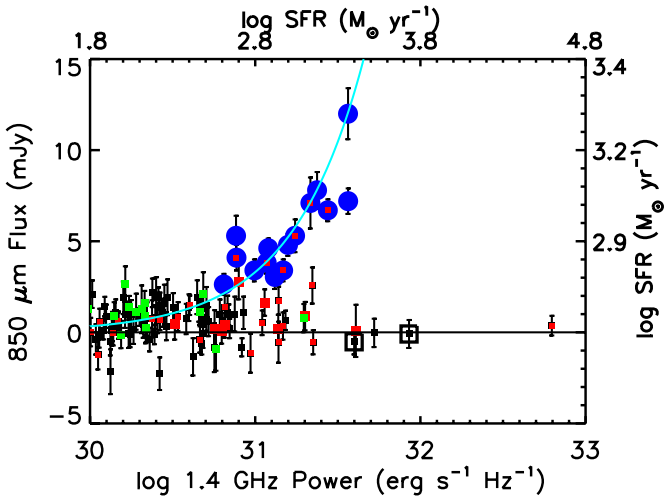

Figure 21. 850 μm flux vs. radio power for the radio sources with spectroscopic, photometric, or CO redshifts $z > 1$ in the region of the SCUBA-2 image where the rms 850 μm error is <1.5 mJy (black squares). X-ray AGNs are marked with red squares, and X-ray quasars are marked with red large squares. Green squares show radio sources with measured rest-frame EW([O II] λ3727) < 10 Å; only $z < 1.5$ sources can be classified as elliptical galaxies this way. Blue solid circles show single radio sources with >4σ 850 μm counterparts. The sources enclosed in black large squares are sources classified as AGNs by Guidetti et al. (2013). Error bars for all the symbols are $\pm 1\sigma$. The cyan curve shows the submillimeter flux expected for an Arp 220 SED based on Equations (7) and (8). The top axis (right-hand axis) shows the SFR that would correspond to the radio power (submillimeter flux), if the source is powered by star formation.

(A color version of this figure is available in the online journal.)

average, than the radio-derived SFRs. This is well within the uncertainties in the absolute calibration of the SFRs, and we conclude that either method will produce similar results.

5.4. Star Formers in the High Radio Power Population

At high radio powers, the submillimeter detected sources are clearly quite distinct from other radio sources. In Figure 21, we show 850 μm flux versus radio power for the radio sources with spectroscopic, photometric, or CO redshifts $z > 1$ in the region of the SCUBA-2 field where the rms 850 μm noise is less than 1.5 mJy (black squares). We mark radio sources with 850 μm counterparts detected above the 4σ level with blue solid circles. (If there is no SMA observation, then we only mark the source if there is a single radio counterpart within the SCUBA-2 beam.) These SMGs begin to enter at a radio power of $\approx 5 \times 10^{30}$ erg s^{-1} Hz^{-1}, as would be expected for sources with an Arp 220 SED obeying the local FIR–radio correlation (cyan curve), given our 4σ 850 μm flux limit of 2 mJy. (This radio power corresponds to an SFR of $\sim$400 $M_\odot$ yr^{-1}, or an 850 μm flux of 2.5 mJy, assuming the sources are powered by star formation.) We mark X-ray AGNs with red squares and X-ray quasars with red large squares. None of the submillimeter detected sources are X-ray quasars.

Above this radio power, we see a bifurcation, with some sources being undetected in the submillimeter, even at very high radio luminosities, while others follow the FIR–radio track of the cyan curve. We shall refer to the two tracks as submillimeter-blank and submillimeter-bright radio sources, respectively.

Based on the small number of sources with high-resolution radio observations in the field, the submillimeter-bright sources appear to be predominantly extended and star formation dominated. The three submillimeter-bright sources in our radio sample with high-resolution 1.4 GHz observations from

either the Multi-Element Radio Linked Interferometer Network (MERLIN)+VLA (Chapman et al. 2004b) or the Very Long Baseline Interferometer (Momjian et al. 2010) have all been confirmed as being extended (CDFN9/GOODS 850-3/GN6, CDFN7/GOODS 850-36, and CDFN3/GN20). (Note that CDFN3/GN20 lies outside the area shown in Figure 21, but it lies smoothly on the submillimeter-bright track.)

Two submillimeter-blank sources in our radio sample at $z > 1$ were classified as AGNs by Guidetti et al. (2013) using high-resolution 5 GHz observations with e-MERLIN combined with existing 1.4 GHz MERLIN+VLA observations obtained by Muxlow et al. (2005). We show these enclosed in black large squares in Figure 21. (A further three of the submillimeter-blank sources shown in Figure 21 were observed by Guidetti et al. but were not clearly classified.)

We shall assume in the following that the submillimeter-bright sources are star formation dominated, though the number of sources used to come to this conclusion is small.

6. STAR FORMATION RATE DISTRIBUTION FUNCTION

A major goal of this paper is to search for evidence of a turn-down in the SFR distribution function, which would indicate a characteristic maximum SFR in galaxies. Here, we use the SCUBA-2 sample of Table 1 to explore the shape of the SFR distribution function at high redshifts.

Of the 49 SCUBA-2 sources in Table 1, 24 have SMA observations that directly determine the radio counterparts. Of these SCUBA-2 sources, 3 have multiple SMA/radio counterparts, giving a total of 27 SMA detected sources. These correspond to all but two of the sources in the SMA sample of Table 2; i.e., GOODS 850-13a and GOODS 850-13c are not included in the SCUBA-2 selection, because they lie below the detection threshold. There are a further 18 SCUBA-2 sources for which there is only a single radio source within the SCUBA-2 beam, which we take to be the counterpart. Four SCUBA-2 sources have multiple radio sources within the beam. Four other SCUBA-2 sources no radio counterparts (including the single SCUBA-2 source/SMA pair CDFN15a and CDFN15b where both SMA counterparts are undetected in the radio, giving a total of five SMGs without radio counterparts). Some of the latter category could be spurious when they are close to the 4σ threshold, but if they are real, as is clearly the case for CDFN15, then they are the most plausible extremely high redshift galaxy candidates.

In the following, we restrict our analysis to the SMGs with well-determined counterparts, giving a total sample of 45 galaxies. (Note, however, that with some reasonable assumptions, we also present results that include the five SMGs without radio counterparts.) Where possible, we use the spectroscopic, photometric, or CO redshifts.

In Figure 22(a), we show radio power (left-hand y-axis) and the SFR calculated from the radio power using Equation (7) (right-hand y-axis) versus redshift for the SMGs at $z > 1$. In Figure 22(b), we show submillimeter flux (left-hand y-axis) and the SFR calculated from the submillimeter flux using Equation (8) (right-hand y-axis) versus redshift for the same sample. We denote sources with spectroscopic, photometric, or CO redshifts with black squares, and we denote sources with millimetric redshifts with blue diamonds. We mark X-ray AGNs with red squares. None of the sources are X-ray quasars. We show the five SMGs without radio counterparts as green right-pointing arrows. We computed the minimum millimetric redshifts for these by assuming a 1.4 GHz flux of 10 μJy.

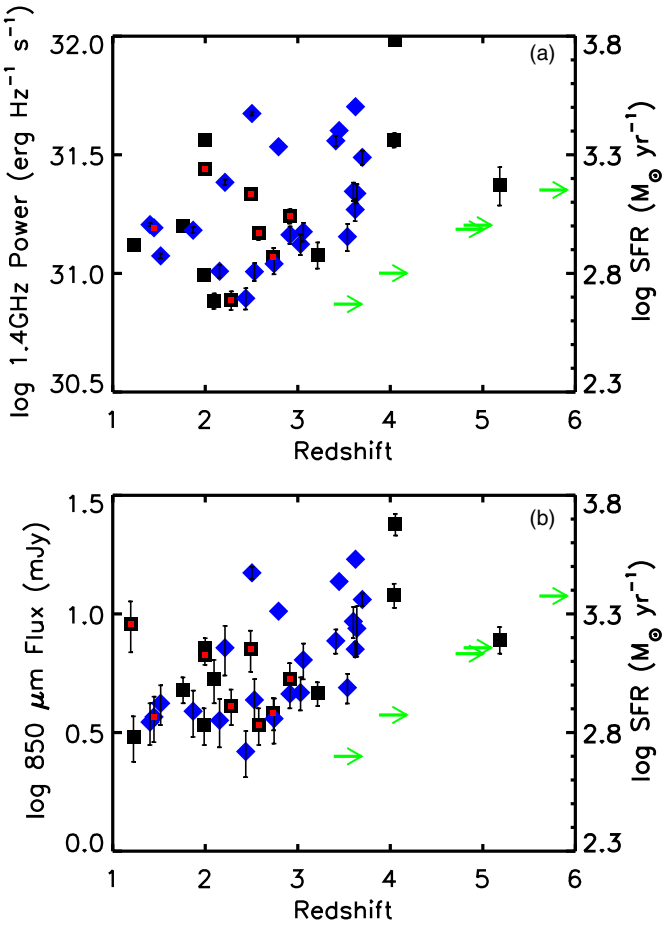

Figure 22. (a) Radio power vs. redshift for the SCUBA-2 sample with well–determined counterparts at $z > 1$ (black squares—spectroscopic, photometric, or CO redshifts; blue diamonds—millimetric redshifts), as well as the five without radio counterparts (green right-pointing arrows; we computed the minimum millimetric redshifts for these by assuming a 1.4 GHz flux of 10 μJy). X-ray AGNs are marked with red squares. None of the sources are X-ray quasars. The right-hand axis shows the SFRs calculated from the radio powers using Equation (7), assuming the sources are powered by star formation. (b) 850 μm flux vs. redshift for the same sample and using the same symbols as in (a). In this panel, the right-hand axis shows the SFRs calculated from the submillimeter fluxes using Equation (8), assuming the sources are powered by star formation. This axis is only valid for sources at $z > 1.5$.

(A color version of this figure is available in the online journal.)

In both panels, the SFRs range from 400 $M_\odot$ yr^{-1} to $\sim$6000 $M_\odot$ yr^{-1}. For homogeneity, we decided to calculate the SFRs from the submillimeter fluxes in our subsequent analysis, but our results are not significantly changed if we instead compute the SFRs from the radio powers.

For each source, we determined the area over which a 4σ detection would have been made in the SCUBA-2 image. We then used this to determine the accessible volume in the redshift interval z1 to z2. Since the conversion from 850 μm flux to SFR is nearly redshift invariant, this is just the comoving volume between z1 and z2 that corresponds to the area for that source. We then formed the SFR per unit volume per log SFR in the redshift interval by summing the inverse volumes and dividing by the bin size width. We used bins stepped by 0.5 in log SFR.

In Figure 23, we show the number density of sources per unit comoving volume per unit log SFR versus log SFR for the $z = 1.5$–6 SCUBA-2 sources with well-determined counterparts (black squares). Here and subsequently, we only

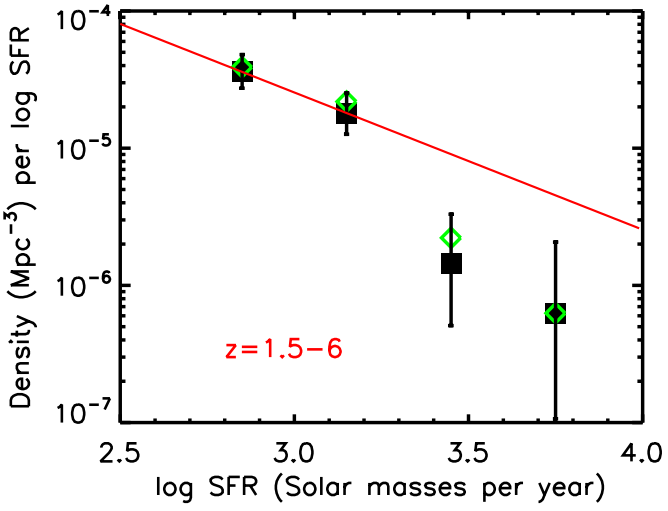

Figure 23. Number density per unit comoving volume per unit log SFR vs. log SFR for the >4σ SCUBA-2 sources at z = 1.5–6 with SFRs > 500 $M_\odot$ yr^{-1}. Black squares show the sources with well-determined counterparts. The error bars are 68% confidence ranges based on the number of sources in each bin. The green diamonds show the results if the five SMGs without radio counterparts are also assumed to lie in this redshift interval. The red solid line shows the shape of the SFR distribution function that would produce equal amounts of star formation in each log SFR interval.

(A color version of this figure is available in the online journal.)

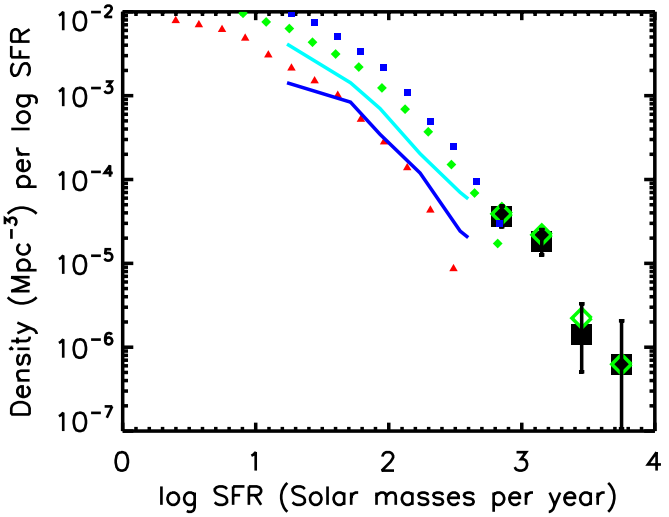

Figure 24. Number density per unit comoving volume per unit log SFR vs. log SFR for the >4σ SCUBA-2 sources at z = 1.5–6 with SFRs > 500 $M_\odot$ yr^{-1}. Black squares show the sources with well–determined counterparts. The error bars are 68% confidence ranges based on the number of sources in each bin. The green diamonds show the results if the five SMGs without radio counterparts are also assumed to lie in this redshift interval. For comparison, the small symbols and curves show extinction-corrected UV results from van der Burg et al. (2010; red triangles—z = 4.8, green diamonds—z = 3.8, blue squares—z = 3.1) and Reddy & Steidel (2009; blue curve—$z \sim 3$, cyan curve—$z \sim 2$), assuming the Kennicutt (1998) conversion of UV luminosity to SFR for a Salpeter IMF.

(A color version of this figure is available in the online journal.)

use the SMGs with SFRs > 500 $M_\odot$ yr^{-1} corresponding to 850 μm fluxes $\gtrsim$3 mJy, where we have substantial area coverage (see Figure 2; this only eliminates two SMGs). The green diamonds show the same but assuming that the five SMGs without radio counterparts also lie in this redshift interval. Because there is no redshift dependence in the SFR conversion (see Equation (8)), the submillimeter fluxes of these sources place them in the appropriate SFR bin. We have not included the three SCUBA-2 sources that have multiple radio sources within the SCUBA-2 beam, but if they also are at z = 1.5–6, then they contain just under 10% of the total submillimeter flux, or, equivalently, of the total SFR. Thus, the overall normalization should not be increased by more than this amount with their inclusion.

The red solid line shows the shape that would be required to produce the same amount of star formation in each logarithmic SFR interval. The two lowest SFR bins fall on this relation; however, above log SFR $\sim$ 3.3, the measured volume density begins to drop below this relation. This drop is highly statistically significant, since a constant amount of star formation in each logarithmic SFR interval would imply that we would have 23 objects above log SFR $\sim$ 3.3 in the field, whereas we see only four. Over the range of the two lowest data points (500–2000 $M_\odot$ yr^{-1}), the total SFR density is 0.016 $M_\odot$ yr^{-1} Mpc^{-3}, while the contribution from sources with SFRs above 2000 $M_\odot$ yr^{-1} is only 0.004 $M_\odot$ yr^{-1} Mpc^{-3}. Thus, we appear to have a characteristic maximum SFR of $\sim$2000 $M_\odot$ yr^{-1}.

It is unlikely that this result could be affected by gravitational lensing of the submillimeter/1.4 GHz sources. While the bright end sources in ultra-wide fields surveys are dominated by lensed sources (Negrello et al. 2010), there is only a low probability of seeing a significantly lensed source in a field of the present size (e.g., Takahashi et al. 2011). We searched around the brightest SMGs for neighboring bright foreground galaxies that could be plausible lensers and found only two. One of these is HDF850.1 (Hughes et al. 1998) or GOODS 850-1, which has a nearby elliptical galaxy at z = 1.224 from Barger et al. (2008). Walter et al. (2012), using their new redshift and position for the SMG from the IRAM Plateau de Bure Interferometer, derived only a modest possible amplification factor of $\sim$1.4.

We can compare the contributions that we found from the very massively star-forming galaxies in the SCUBA-2 sample to the contributions from rest-frame UV selected samples. In Figure 24, we plot volume density versus log SFR for the SMGs from Figure 23 and for Lyman break galaxy (LBGs) from the extinction-corrected UV luminosity functions of van der Burg et al. (2010; red triangles for z = 4.8, green diamonds for z = 3.8, and blue squares for z = 3.1) and Reddy & Steidel (2009; blue curve for $z \sim 3$ and cyan curve for $z \sim 2$). We converted their luminosity functions to the units of Figure 24 using the Kennicutt (1998) conversion of 1600 Å luminosity to SFR for a Salpeter IMF.

van der Burg et al. (2010) adopted luminosity-dependent dust correction factors from Bouwens et al. (2009). Reddy & Steidel (2009) also used luminosity-dependent dust corrections, but theirs were significantly smaller. Indeed, van der Burg et al. directly compared their extinction-corrected SFR densities with those of Reddy & Steidel in their Figure 14 and found them to be quite different, illustrating the level of uncertainty in the extinction corrections.

While the distribution of SMG SFRs appears to extend smoothly from the distribution of LBG SFRs, the LBG SFRs determined from the extinction-corrected UV selected samples are not as high as those of the SMGs but instead cut off at $\sim$300 $M_\odot$ yr^{-1}. Thus, either the SMGs are completely omitted from the UV selected samples, or the extinction corrections applied to some UV sources are substantially underestimated (see discussion in Bouwens et al. 2009). Even if catastrophically wrong extinction corrections are applied to some UV sources,

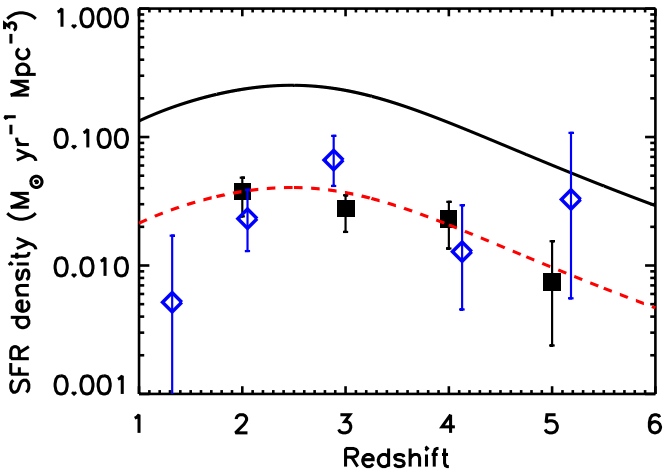

Figure 25. SFR density per unit comoving volume vs. redshift for the SCUBA-2 sample with SFRs $> 500\ M_\odot\ \mathrm{yr}^{-1}$. The black squares show the computations at $z = 1.5$–2.5, 2.5–3.5, 3.5–4.5, and 4.5–5.5 and are plotted at the mean redshift of each bin. Sources without radio counterparts are placed at their minimum millimetric redshifts, and we have renormalized the points by a multiplicative factor of 1.1 to allow for the sources with multiple radio counterparts. The error bars are 68% confidence ranges based on the number of sources in the bin. The black solid curve shows the SFR density history computed by Hopkins & Beacom (2006) based on UV selected samples, and the red dashed curve shows this multiplied by 0.16 to match roughly the SFR density history of the current sample. The blue open diamonds show the SFR density history computed by Barger et al. (2012) based on the smaller SCUBA sample in the GOODS-N field. We have reduced these points by a factor of 1.4 to correspond to the present SFR calibration.

(A color version of this figure is available in the online journal.)

causing lower SFRs to be assigned to sources that genuinely have high SFRs, the UV distributions in Figure 24 would remain the same. The reason is that the volume density of SMGs is much smaller than that of LBGs, which means the number of sources that would be affected would be too small to make a difference.

Since the LBGs' brightest submillimeter fluxes are only ~0.2–0.3 mJy based on stacking analyses (e.g., Peacock et al. 2000; Chapman et al. 2000; Webb et al. 2003), with the present submillimeter sensitivities, which are set by the blank field confusion limit, the SMG SFRs do not overlap with LBG SFRs. Thus, there is a gap between the two populations where the SFR distribution function is poorly determined.

In Figure 25, we plot the SFR density per unit comoving volume for the SCUBA-2 sample with SFRs $> 500\ M_\odot\ \mathrm{yr}^{-1}$ (black squares) versus redshift and compare it with the compilation by Hopkins & Beacom (2006; black solid curve) for extinction-corrected UV selected samples over the same redshift range. We compare these results with the SFR density history of Barger et al. (2012)—who used a substantially smaller SCUBA selected and SMA confirmed sample in the GOODS-N—after reducing their points by a factor of 1.4 (blue open squares) to adjust them to the SFR calibration of the present paper. Note that Casey et al. (2013) constructed the most recent SFR density history using both 450 μm and 850 μm selected SCUBA-2 samples in the COSMOS field, which they compared with Barger et al. (2012) at 850 μm, Chapman et al. (2005) at 850 μm using SCUBA, Wardlow et al. (2011) at 870 μm using LABOCA, Roseboom et al. (2012) at 1.2 mm using MAMBO, and Casey et al. (2012a, 2012b) at 250–500 μm using *Herschel*-SPIRE (see their Figure 14).

With our relatively large sample, we see a smoother evolution than we saw in Barger et al. (2012), and one which closely matches the shape of the Hopkins & Beacom (2006) SFR density history. The massive star-forming galaxies studied in this paper contain about 16% of the SFR density seen in the UV selected population (the red dashed curve shows a scaled down version of Hopkins & Beacom), though the systematic uncertainties in the SFR determinations and in the UV extinction corrections could easily change this by multiplicative factors of two. As we saw from Figure 24, the contributions are essentially disjoint, and the SMG contributions should be added to the extinction-corrected UV contributions.

The fraction of the total star formation in galaxies with SFRs $> 500\ M_\odot\ \mathrm{yr}^{-1}$ is substantially higher than what was found by Rodighiero et al. (2011) using a *Herschel*-PACS selection, which suggests that the longer wavelength samples of the present paper are more effective at finding these galaxies. Indeed, only 13 of the 27 SMA detected sources lying in the GOODS-*Herschel* region (which have exact positions and confirmed 850 μm fluxes) are detected above the 4σ threshold in the PACS 100 μm image.

The combined extinction-corrected UV and submillimeter data in Figure 25 show that the shape of the SFR density does not change much in the redshift range $z = 1.5$–5.5, though there is about a factor of three increase in the absolute normalization at $z = 2$ relative to that at $z = 5$.

7. DISCUSSION

In this discussion, our goal is to fit together the various pieces of information that we have presented in this paper to form a comprehensive picture. From Figure 23, we saw a turn-down in the SFR distribution function for SFRs above 2000 $M_\odot\ \mathrm{yr}^{-1}$. However, even 2000 $M_\odot\ \mathrm{yr}^{-1}$ is an extraordinarily high SFR, and we aim to show that this rate cannot be sustained for any long period ($\gg 10^8$ yr) in individual galaxies without producing too many ultra-massive galaxies overall.

Under the simple assumption that all the SCUBA-2 galaxies have a fixed time period of star formation, τ, that does not depend on luminosity or redshift, then each galaxy forms a mass $M = \tau \times$ SFR. We obtain the number density by integrating the SFR distribution function (Figure 23) over cosmic time and dividing by τ. To make the integration, we assume that the shape of the SFR distribution function is fixed with redshift, but we allow the normalization to vary with redshift in order to match the shape of the red dashed curve in Figure 25.

In Figure 26, we plot the mass distribution function at $z = 2.5$–3 that we predict using two values of τ, 10^8 yr (squares) and 5×10^8 yr (diamonds). We compare these with the mass distribution function determined by Ilbert et al. (2013) using the UltraVISTA DR1 data release for the same redshift interval, after correcting theirs to a Salpeter IMF (red curve). Longer star-forming lifetimes than 10^8 yr greatly over-predict the high-mass end of the mass distribution. This is also consistent with the measured gas reservoirs in the SMGs, which are only large enough to sustain such high SFRs for a limited length of time. For example, for GN20, Hodge et al. (2012, 2013a) give a CO based mass of $1.3 \times 10^{11}\ M_\odot$ and a dynamical mass of $5.4 \times 10^{11}\ M_\odot$, which could only sustain GN20's high SFR for a short period.

Thus, there are many generations of high SFR galaxies contributing to the SFR distribution function through the redshift interval that are continuously switching on, forming a massive galaxy, and then switching off. Correspondingly, there will be a wide range of ages in the most massive galaxies at any redshift. However, at later redshifts, the distribution of ages will be centered around a more mature age.

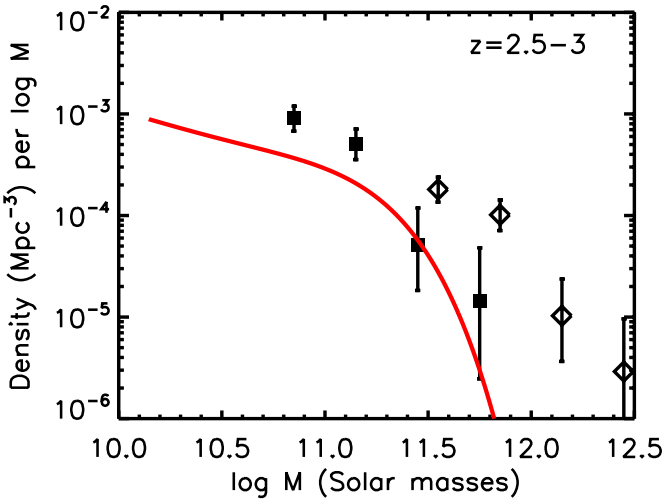

Figure 26. Mass density per unit comoving volume per unit log M vs. log M for $z = 2.5$–3, computed from the SFR distribution function of Figure 23 assuming a fixed shape with redshift but allowing the normalization to vary. The open diamonds (black squares) show the values calculated if each SFR episode lasts for 5×10^8 yr (10^8 yr). The red curve shows the mass distribution function of Ilbert et al. (2013) in this redshift interval corrected to a Salpeter IMF.

(A color version of this figure is available in the online journal.)

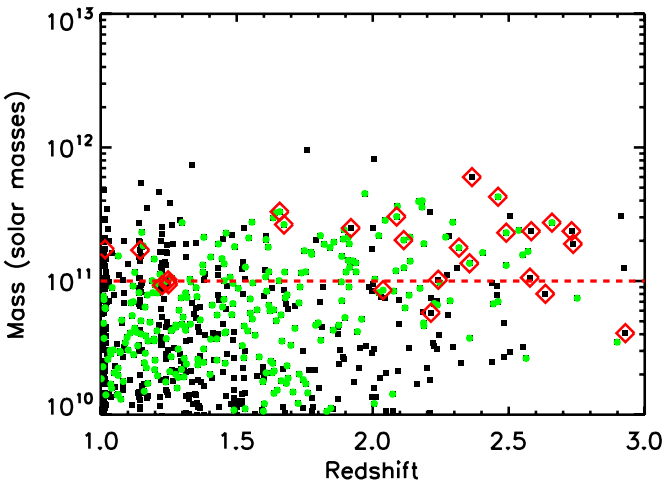

Figure 27. Mass vs. redshift in the GOODS-N region. Black squares denote spectroscopic redshifts, and green circles denote photometric redshifts. The red diamonds mark high radio power sources ($P_{1.4\,\mathrm{GHz}} \geqslant 10^{31}$ erg s^{-1} Hz^{-1}). The red dashed line shows the 10^{11} $M_\odot$ limit.

(A color version of this figure is available in the online journal.)

The $K - z$ relation shows that nearly all high-redshift radio sources lie in very massive galaxies. The most powerful radio sources lie in galaxies with stellar masses $>10^{12}$ $M_\odot$, which must have formed at high redshifts ($z \gg 5$) (Willott03; Rocca-Volmerange et al. 2004). However, the mass dependence on radio power is extremely weak. We find that even sources 1000–10,000 times less powerful in the radio than the sources considered in Willott03 must lie in galaxies with masses in excess of 10^{11} $M_\odot$. Such galaxies are moderately rare at all redshifts and lie on the exponential tail of the mass distribution function (see Figure 26).

However, approaching this from the other direction, we also find that a substantial fraction of high-mass galaxies contain powerful radio sources. We show the mass versus redshift relation for galaxies in the GOODS-N region in Figure 27. We calculated the masses following Cowie & Barger (2008) and using a Salpeter IMF. We mark the galaxies with spectroscopic redshifts with black squares and the galaxies with photometric redshifts with green circles. We enclose the galaxies with high radio powers ($P_{1.4\,\mathrm{GHz}} \geqslant 10^{31}$ erg s^{-1} Hz^{-1}) in red diamonds.

As expected from the $K - z$ relation, nearly all the high radio power sources have galaxy masses $>10^{11}$ $M_\odot$. In the other direction, above $z = 2$, $34\% \pm 11\%$ of the galaxies satisfying this mass limit contain high radio power sources. Thus, the integrated lifetime of the powerful radio period must be long. At $z = 2$, the age of the universe is 3.2×10^9 yr, and in order to have one-third of the massive galaxies be powerful radio sources, this phase (or phases) must have a lifetime in excess of 10^9 yr.

The relative timescales of the star-forming period (10^8 yr or less) relative to that of the radio-powerful AGN period(s) (in excess of 10^9 yr) imply that, at least at $z \sim 2$, ~10% of the high radio power sources will be star formers. This is roughly consistent with the fraction that we determined in Section 5.1 (13%–16%). Thus, after the $>10^{11}$ $M_\odot$ galaxies form in the short initial starburst, they spend a substantial fraction of their subsequent lifetime as high radio power AGNs.

8. SUMMARY

In this paper, we presented an integrated SCUBA-2, SMA, and 1.4 GHz study of a 400 arcmin^2 area surrounding the GOODS-N field. Using the SCUBA-2 data, we constructed an 850 μm catalog of 49 sources to 2 mJy (4σ). We looked for counterparts to these sources in the ultradeep (11.5 μJy at 5σ) radio data. In cases where there were multiple radio counterparts, we often were able to use new and existing SMA data to determine the correct counterparts (the correct radio counterparts to only four SMGs remain uncertain). Only five SMGs have no radio counterparts, making them extremely high redshift galaxy candidates.

We either obtained ourselves or located in the literature extensive spectroscopic redshifts for the radio sources in the field. In the GOODS-N proper, the redshift identifications are highly complete to $K_s = 21$ after including a small number of photometric redshifts. For the SMGs without spectroscopic, CO, or photometric redshifts, we used an Arp 220 based model from Barger et al. (2000) to measure millimetric redshifts from the 1.4 GHz to 860 μm flux ratios. The millimetric redshifts predominantly fill in the $z \sim 2.5$–4 range.

We found an extended tail of radio sources with faint optical/NIR counterparts, the faintest of which are undetected even in the *HST* ACS images. These sources are not identifiable with optical/NIR spectroscopy or photometry and may lie at high redshifts. Indeed, we found that there is a strong correlation between K_s magnitude and redshift in the radio sample (the $K - z$ relation), making it possible to use the K_s magnitudes as a crude redshift estimator for the radio sources.

We computed rest-frame radio power for the radio sources with spectroscopic, CO, or photometric redshifts. At $z \gtrsim 3$, even these ultradeep observations are only sensitive to sources brighter than the ULIRG limit calculated assuming the FIR–radio correlation.

We are particularly interested in the high radio power ($P_{1.4\,\mathrm{GHz}} \geqslant 10^{31}$ erg s^{-1} Hz^{-1}) sources at high redshifts, as those at $z < 1.5$ mostly appear to be AGN powered. At $z > 1.5$, a substantial fraction (37%) of the spectroscopically identified high radio power sources are detected in the submillimeter, suggesting that they are massive star formers. However, it is difficult

to determine the true fraction of high radio power star formers, because there are strong selection effects in the spectroscopic identifications of the radio sources at high redshifts. Based on the $K - z$ relation, the unidentified radio sources at $K_s > 21$ should lie at high redshifts. Using the 850 μm S/N for the high radio power sources at these magnitudes, we found a likely star-forming fraction of 13%–16%.

We computed SFRs for the individual sources from the 1.4 GHz power, assuming that the FIR–radio correlation is roughly invariant to $z \sim 6$ for SMGs down to our 850 μm flux threshold of 2 mJy, and from the submillimeter fluxes, assuming using an SFR conversion computed from the average SEDs of isolated galaxies in the sample. (The SFR conversion is quite close to that which would be computed from Arp 220.) We found that the SFRs derived from the two methods are in good agreement for the sources with spectroscopic, CO, or photometric redshifts $z > 1.5$, though the submillimeter derived SFRs are about 5% higher, on average, than the radio derived SFRs. This is well within the uncertainties in the absolute calibration of the SFRs.

We found that at high radio powers, the submillimeter detected sources are quite distinct from the other radio sources. A small number of these had high-resolution radio observations that showed them to be predominantly extended or star formation dominated, so we assumed that they were all star formation dominated.

We found that the SFRs of the SMGs ranged from 400 $M_\odot$ yr^{-1} to ~6000 $M_\odot$ yr^{-1}. We constructed the SFR distribution function for the SMGs at $z > 1.5$ with SFRs > 500 $M_\odot$ yr^{-1} and found a characteristic maximum SFR of ~2000 $M_\odot$ yr^{-1}. It should be emphasized that while we only have spectroscopic redshifts for about 40% of the sources, and the remaining sources have relatively uncertain redshifts primarily based on the radio to submillimeter flux, the results are very insensitive to even fairly large errors in the redshifts. Because the conversion from 850 μm flux depends extremely weakly on redshift at $z > 1.5$, the result would only change if an SMG was moved outside this redshift interval by the redshift uncertainty.

We compared our submillimeter results with extinction-corrected UV selected samples and saw that the LBGs do not have as high of SFRs as the SMGs but instead cut off at ~300 $M_\odot$ yr^{-1}. Thus, the two samples are essentially disjoint.

We constructed the SFR density history for the SMG sample and compared it with the extinction-corrected UV selected SFR density history compilation of Hopkins & Beacom (2006) over the redshift range $z = 1$–6. The shapes closely match, with the SMG SFR density history being about 16% of the extinction-corrected UV selected SFR density history. However, since the samples are disjoint, the SMG contributions and the extinction-corrected UV contributions should be added for a fuller accounting of the overall star formation history.

Finally, we discussed how the above information could be put together to form a comprehensive picture. We concluded that nearly all high radio power sources have galaxy masses $>10^{11}$ $M_\odot$ and that in order to avoid over-predicting the high galaxy mass end, there must be many generations of high SFR galaxies that are continuously switching on, forming a massive galaxy in a period of $<10^8$ yr, and then switching off. However, the powerful radio period lasts much longer ($>10^9$ yr), making the high radio power sources without submillimeter counterparts the most common type of high radio power source, even at high redshift.

We thank the anonymous referee for a thoughtful report. We gratefully acknowledge support from the University of Wisconsin Research Committee with funds granted by the Wisconsin Alumni Research Foundation and the David and Lucile Packard Foundation (A. J. B.), NSF grants AST-1313150 (A. J. B.), AST-0709356 (L. L. C., C.-C. C.), and AST-1313309 (L. L. C.), and National Science Council of Taiwan grant 102-2119-M-001-007-MY3 (W.-H. W.). C. M. C. was generously supported by a Hubble Fellowship provided by Space Telescope Science Institute, grant HST-HF-51268.01-A. We acknowledge the cultural significance that the summit of Mauna Kea has to the indigenous Hawaiian community.

REFERENCES

Alexander, D. M., Bauer, F. E., Brandt, W. N., et al. 2003, AJ, 126, 539
Archibald, E. N., Dunlop, J. S., Hughes, D. H., et al. 2001, MNRAS, 323, 417
Barger, A. J., Cowie, L. L., Brandt, W. N., et al. 2002, AJ, 124, 1839
Barger, A. J., Cowie, L. L., Capak, P., et al. 2003, AJ, 126, 632
Barger, A. J., Cowie, L. L., Mushotzky, R. F., et al. 2005, AJ, 129, 578
Barger, A. J., Cowie, L. L., & Richards, E. A. 2000, AJ, 119, 2092
Barger, A. J., Cowie, L. L., & Wang, W.-H. 2007, ApJ, 654, 764
Barger, A. J., Cowie, L. L., & Wang, W.-H. 2008, ApJ, 689, 687
Barger, A. J., Wang, W.-H., Cowie, L. L., et al. 2012, ApJ, 761, 89
Bell, E. F. 2003, ApJ, 586, 794
Berta, S., Magnelli, B., Nordon, R., et al. 2011, A&A, 532, 49
Best, P. N., & Heckman, T. M. 2012, MNRAS, 421, 1569
Blain, A. W., & Longair, M. S. 1993, MNRAS, 264, 509
Bothwell, M. S., Chapman, S. C., Tacconi, L., et al. 2010, MNRAS, 405, 219
Bouwens, R. J., Illingworth, G. D., Franx, M., et al. 2009, ApJ, 705, 936
Brammer, G. B., van Dokkum, P. G., & Coppi, P. 2008, ApJ, 686, 1503
Brookes, M. H., Best, P. N., Peacock, J. A., Röttgering, H. J. A., & Dunlop, J. S. 2008, MNRAS, 385, 1297
Bryant, J. J., Johnston, H. M., Broderick, J. W., et al. 2009, MNRAS, 395, 1099
Carilli, C. L., & Yun, M. S. 1999, ApJL, 513, L13
Casey, C. M. 2012, MNRAS, 425, 3094
Casey, C. M., Berta, S., Béthermin, M., et al. 2012a, ApJ, 761, 139
Casey, C. M., Berta, S., Béthermin, M., et al. 2012b, ApJ, 761, 140
Casey, C. M., Chen, C.-C., Cowie, L. L., et al. 2013, MNRAS, 436, 1919
Chabrier, G. 2003, PASP, 115, 763
Chapman, S. C., Blain, A. W., Ivison, R. J., & Smail, I. R. 2003, Natur, 422, 695
Chapman, S. C., Blain, A. W., Smail, I., & Ivison, R. J. 2005, ApJ, 622, 772
Chapman, S. C., Scott, D., Steidel, C. C., et al. 2000, MNRAS, 319, 318
Chapman, S. C., Smail, I., Blain, A. W., & Ivison, R. J. 2004a, ApJ, 614, 671
Chapman, S. C., Smail, I., Windhorst, R., Muxlow, T., & Ivison, R. J. 2004b, ApJ, 611, 732
Chen, C.-C., Cowie, L. L., Barger, A. J., et al. 2013, ApJ, 776, 131
Chen, C.-C., Cowie, L. L., Wang, W.-H., Barger, A. J., & Williams, J. P. 2011, ApJ, 733, 64
Cohen, J. G., Hogg, D. W., Blandford, R., et al. 2000, ApJ, 538, 29
Condon, J. J. 1989, ApJ, 338, 13
Condon, J. J. 1992, ARA&A, 30, 575
Condon, J. J., Anderson, M. L., & Helou, G. 1991, ApJ, 376, 95
Condon, J. J., Kellermann, K. I., Kimball, A. E., Ivezić, Ž, & Perley, R. A. 2013, ApJ, 768, 37
Cooper, M. C., Aird, J. A., Coil, A. L., et al. 2011, ApJS, 193, 14
Cowie, L. L., & Barger, A. J. 2008, ApJ, 686, 72
Cowie, L. L., Barger, A. J., Fomalont, E. B., & Capak, P. 2004a, ApJL, 603, L69
Cowie, L. L., Barger, A. J., Hu, E. M., Capak, P., & Songaila, A. 2004b, AJ, 127, 3137
Cowie, L. L., Barger, A. J., & Hu, E. M. 2011, ApJ, 738, 136
Cowie, L. L., Barger, A. J., Wang, W.-H., & Williams, J. P. 2009, ApJL, 697, L122
Cowie, L. L., Songaila, A., Hu, E. M., & Cohen, J. G. 1996, AJ, 112, 839

Daddi, E., Dannerbauer, H., Krips, M., et al. 2009a, ApJL, 695, L176
Daddi, E., Dannerbauer, H., Stern, D., et al. 2009b, ApJ, 694, 1517
De Breuck, C., van Breugel, W., Stanford, S. A., et al. 2002, AJ, 123, 637
Dempsey, J. T., Friberg, P., Jenness, T., et al. 2013, MNRAS, 430, 2534
Dunlop, J. S. 2002, in ASP Conf. Ser. 283, A New Era in Cosmology, ed. T. Shanks & N. Metcalfe (San Francisco, CA: ASP), 381
Dunlop, J. S., Hughes, D. H., Rawlings, S., Eales, S. A., & Ward, M. J. 1994, Natur, 370, 347
Eales, S., Rawlings, S., Law-Green, D., Cotter, G., & Lacy, M. 1997, MNRAS, 291, 593
Elbaz, D., Dickinson, M., Hwang, H. S., et al. 2011, A&A, 533, 119
Faber, S. M., Phillips, A. C., Kibrick, R. I., et al. 2003, Proc. SPIE, 4841, 1657
Giavalisco, M., Dickinson, M., Ferguson, H. C., et al. 2004, ApJL, 600, L93
Guidetti, D., Bondi, M., Prandoni, I., et al. 2013, MNRAS, 432, 2798
Hatsukade, B., Iono, D., Akiyama, T., et al. 2010, ApJ, 711, 974
Helou, G., Soifer, B. T., & Rowan-Robinson, M. 1985, ApJL, 298, L7
Ho, P. T. P., Moran, J. M., & Lo, K. Y. 2004, ApJL, 616, L1
Hodge, J. A., Carilli, C. L., Walter, F., Daddi, E., & Riechers, D. 2013a, ApJ, 776, 22
Hodge, J. A., Carilli, C. L., Walter, F., et al. 2012, ApJ, 760, 11
Hodge, J. A., Karim, A., Smail, I., et al. 2013b, ApJ, 768, 91
Holland, W. S., Bintley, D., Chapin, E. L., et al. 2013, MNRAS, 430, 2513
Holland, W. S., Robson, E. I., Gear, W. K., et al. 1999, MNRAS, 303, 659
Hopkins, A. M., & Beacom, J. F. 2006, ApJ, 651, 142
Hughes, D. H., Serjeant, S., Dunlop, J., et al. 1998, Natur, 394, 241
Ibar, E., Ivison, R. J., Best, P. N., et al. 2010, MNRAS, 401, L53
Ilbert, O., McCracken, H. J., Le Fèvre, O., et al. 2013, A&A, 556, A55
Iono, D., Peck, A. B., Pope, A., et al. 2006, ApJL, 640, L1
Ivison, R. J., Dunlop, J. S., Hughes, D. H., et al. 1998, ApJ, 494, 211
Jarvis, M. J., Rawlings, S., Eales, S., et al. 2001, MNRAS, 326, 1585
Karim, A., Swinbank, A. M., Hodge, J., et al. 2013, MNRAS, 432, 2
Kennicutt, R. C. 1998, ApJ, 498, 541
Klaas, U., Haas, M., Heinrichsen, I., & Schulz, B. 1997, A&A, 325, L21
Knudsen, K. K., Kneib, J.-P., Richard, J., Petitpas, G., & Egami, E. 2010, ApJ, 709, 210
Kroupa, P. 2001, MNRAS, 322, 231
Lacy, M., Bunker, A. J., & Ridgway, S. E. 2000, AJ, 120, 68
Lagache, G., Puget, J.-L., & Dole, H. 2005, ARA&A, 43, 727
Laing, R. A., Riley, J. M., & Longair, M. S. 1983, MNRAS, 204, 151
Larson, D., Dunkley, J., Hinshaw, G., et al. 2011, ApJS, 192, 16
Lilly, S. J., & Longair, M. S. 1984, MNRAS, 211, 833
Magnelli, B., Lutz, D., & Santini, P. 2012, A&A, 539, 155
Magnelli, B., Popesso, P., Berta, S., et al. 2013, A&A, 553, 132
Momjian, E., Wang, W.-H., Knudsen, K. K., et al. 2010, AJ, 139, 1622
Moran, E. C., Lehnert, M. D., & Helfand, D. J. 1999, ApJ, 526, 649
Muxlow, T. W. B., Richards, A. M. S., Garrington, S. T., et al. 2005, MNRAS, 358, 1159
Negrello, M., Hopwood, R., De Zotti, G., et al. 2010, Sci, 380, 800
Oke, J. B., Cohen, J. G., Carr, M., et al. 1995, PASP, 107, 375
Peacock, J. A., Rowan-Robinson, M., Blain, A. W., et al. 2000, MNRAS, 318, 535
Perera, T. A., Chapin, E. L., Austermann, J. E., et al. 2008, MNRAS, 391, 1227
Pope, A., Borys, C., Scott, D., et al. 2005, MNRAS, 358, 149
Pope, A., Ranga-Ram, C., Alexander, D. M., et al. 2008, ApJ, 675, 1171
Rafferty, D. A., Brandt, W. N., Alexander, D. M., et al. 2011, ApJ, 742, 3
Reddy, N. A., Dickinson, M., Elbaz, D., et al. 2012, ApJ, 744, 154
Reddy, N. A., & Steidel, C. C. 2009, ApJ, 692, 778
Reddy, N. A., Steidel, C. C., Erb, D. K., Shapley, A. E., & Pettini, M. 2006, ApJ, 653, 1004
Reuland, M., Röttgering, H., van Breugel, W., & De Breuck, C. 2004, MNRAS, 353, 377
Richards, E. A. 2000, ApJ, 533, 611
Rocca-Volmerange, B., Le Borgne, D., De Breuck, C., Fioc, M., & Moy, E. 2004, A&A, 415, 931
Rodighiero, G., Daddi, E., Baronchelli, I., et al. 2011, ApJL, 739, L40
Roseboom, I. G., Ivison, R. J., Grève, T. R., et al. 2012, MNRAS, 419, 2758
Sadler, E. M., Jackson, C. A., Cannon, R. D., et al. 2002, MNRAS, 329, 227
Sadler, E. M., Jenkins, C. R., & Kotanyi, C. G. 1989, MNRAS, 240, 591
Salpeter, E. E. 1955, ApJ, 121, 161
Serjeant, S., Dunlop, J. S., Mann, R. G., et al. 2003a, MNRAS, 344, 887
Serjeant, S., Dye, S., Mortier, A., et al. 2008, MNRAS, 386, 1907
Serjeant, S., Farrah, D., Geach, J., et al. 2003b, MNRAS, 346, L51
Simpson, C., Rawlings, S., Ivison, R., et al. 2012, MNRAS, 421, 3060
Smolčić, V., Aravena, M., Navarrete, F., et al. 2012, A&A, 548, 4
Swinbank, A. M., Smail, I., Chapman, S. C., et al. 2004, ApJ, 617, 64
Takahashi, R., Oguri, M., Sato, M., & Hamana, T. 2011, ApJ, 742, 15
Treu, T., Ellis, R. S., Liao, T. X., et al. 2005, ApJL, 622, L5
Trouille, L., Barger, A. J., Cowie, L. L., Yang, Y., & Mushotzky, R. F. 2008, ApJS, 179, 1
van der Burg, R. F. J., Hildebrandt, H., & Erben, T. 2010, A&A, 523, A74
Walter, F., Decarli, R., Carilli, C., et al. 2012, Natur, 486, 233
Wang, W.-H., Cowie, L. L., & Barger, A. J. 2004, ApJ, 613, 655
Wang, W.-H., Cowie, L. L., & Barger, A. J. 2006, ApJ, 647, 74
Wang, W.-H., Cowie, L. L., Barger, A. J., Keenan, R. C., & Ting, H.-C. 2010, ApJS, 187, 251
Wang, W.-H., Cowie, L. L., Barger, A. J., & Williams, J. P. 2011, ApJL, 726, L18
Wang, W.-H., Cowie, L. L., van Saders, J., Barger, A. J., & Williams, J. P. 2007, ApJL, 670, L89
Wardlow, J. L., Smail, I., Coppin, K. E. K., et al. 2011, MNRAS, 415, 1479
Webb, T. M., Eales, S., Foucaud, S., et al. 2003, ApJ, 582, 6
Willott, C. J., Rawlings, S., Jarvis, M. J., & Blundell, K. M. 2003, MNRAS, 339, 173
Wirth, G. D., Willmer, C. N. A., Amico, P., et al. 2004, AJ, 127, 3121
Younger, J. D., Dunlop, J. S., Peck, A. B., et al. 2008a, MNRAS, 387, 707
Younger, J. D., Fazio, G. G., Wilner, D. J., et al. 2008b, ApJ, 688, 59
Zezas, A. L., Georgantopoulos, I., & Ward, M. J. 1998, MNRAS, 301, 915